Neuroscience

The Journal of Physiology

Active dendrites mediate stratified gamma-range coincidence detection in hippocampal model neurons

Anindita Das and Rishikesh Narayanan

Cellular Neurophysiology Laboratory, Molecular Biophysics Unit, Indian Institute of Science, Bangalore, India

Key points

- Quantitative metrics for the temporal window of integration/coincidence detection, based on the spike-triggered average, were employed to assess the emergence and dependence of gamma-range coincidence detection in hippocampal pyramidal neurons on various ion channel combinations.
- The presence of hyperpolarization-activated cyclic nucleotide-gated (HCN) channels decreased the coincidence detection window (CDW) of the neuronal compartment to the gamma frequency range. Interaction of HCN channels with T-type calcium channels and persistent sodium channels further reduced the CDW, whereas interaction with A-type potassium channels broadened the CDW.
- When multiple channel gradients were co-expressed, the high density of resonating conductances in the distal dendrites led to a slow gamma CDW in the proximal dendrites and a fast-gamma CDW in the distal dendrites.
- The presence of resonating and spike-generating conductances serve as a mechanism underlying the emergence of stratified gamma-range coincidence detection in the dendrites of CA1 pyramidal neurons, enabling them to perform behaviour- and state-dependent gamma frequency multiplexing.

Abstract Hippocampal pyramidal neurons exhibit gamma-phase preference in their spikes, selectively route inputs through gamma frequency multiplexing and are considered part of gamma-bound cell assemblies. How do these neurons exhibit gamma-frequency coincidence detection capabilities, a feature that is essential for the expression of these physiological observations, despite their slow membrane time constant? In this conductance-based modelling study, we developed quantitative metrics for the temporal window of integration/coincidence detection based on the spike-triggered average (STA) of the neuronal compartment. We employed these metrics in conjunction with quantitative measures for spike initiation dynamics to assess the emergence and dependence of coincidence detection and STA spectral selectivity on various ion channel combinations. We found that the presence of resonating conductances (hyperpolarization-activated cyclic nucleotide-gated or T-type calcium), either independently or synergistically when expressed together, led to the emergence of spectral selectivity in the spike initiation dynamics and a significant reduction in the coincidence detection window (CDW). The presence of A-type potassium channels, along with resonating conductances, reduced the STA characteristic frequency and broadened the CDW, but persistent sodium channels sharpened the CDW by strengthening the spectral selectivity in the STA. Finally, in a morphologically precise model endowed with experimentally constrained channel gradients, we found that somatodendritic compartments expressed functional maps of strong theta-frequency selectivity in spike initiation dynamics and gamma-range CDW. Our results reveal the heavy expression of resonating and spike-generating conductances as the mechanism underlying the robust emergence of stratified gamma-range coincidence detection in the dendrites of hippocampal and cortical pyramidal neurons.

Abbreviations   CaT, T-type Ca^{2+} channel; CDW, coincidence detection window; C_m, specific membrane capacitance; F_X, factor quantifying the somatodendritic fold increase in the density of channel X; f_R, local resonance frequency; f_{STA}, STA characteristic frequency; f_{TR}, transfer resonance frequency; $\bar{g}_X$, maximal HCN conductance of channel X; g_X^{Base}, baseline (somatic) density of channel X; HCN, hyperpolarization-activated cyclic nucleotide-gated channel; I–CD continuum, integrator–coincidence detector continuum; IPI, inter-pulse interval; I_{STA}^{Peak}, positive peak of the spike-triggered average; KA, A-type potassium channel; KDR, delayed rectifier potassium channel; NaF, fast Na^+ channel; NaP, persistent Na^+ channel; Q_{STA}, STA selectivity strength; R_a, specific intracellular resistivity; R_{in}, input resistance; R_m, specific membrane resistivity; σ_{noise}, standard deviation of Gaussian white noise; SPPL, spike-proximal positive lobe; STA, spike-triggered average; STG, spike-triggered conductance; τ_{act}, activation time constant of the channel activation gate; T_{ECDW}, effective coincidence detection window; τ_{inact}, inactivation time constant of the channel inactivation gate; T_{TCDW}, total coincidence detection window; VGIC, voltage-gated ion channel; V_m, membrane potential; ZAP, impedance amplitude profile.

Introduction

Coincidence detection of afferent inputs arriving at higher frequencies is an important physiological characteristic of several classes of pyramidal neurons. This pivotal neurophysiological feature has far-reaching implications that include gamma-phase preference of neuronal spikes, read-out of cell assemblies that are organized within a single gamma cycle, induction of neuronal plasticity, selective routing of inputs through frequency multiplexing and binding of distributed responses from several neural structures (Softky, 1994; Magee & Johnston, 1997; Singer *et al.* 1997; Stuart & Häusser, 2001; Fries *et al.* 2007; Senior *et al.* 2008; Colgin *et al.* 2009; Buzsaki, 2010; Colgin & Moser, 2010; Wang, 2010; Buzsaki & Wang, 2012; Lisman & Jensen, 2013; Bieri *et al.* 2014). Although the roles of specific dendritic conductances in mediating high-frequency coincidence detection, especially in the auditory system, have been analysed (Softky, 1994; Agmon-Snir *et al.* 1998; Joris *et al.* 1998; Golding & Oertel, 2012; Meng *et al.* 2012), a systematic analysis of what mediates gamma-frequency coincidence detection in hippocampal neurons has been lacking. This understanding becomes especially critical in the dendrites of pyramidal neurons that receive a barrage of stratified synaptic inputs that are processed differentially based on their anatomical origin and temporal features, thereby promoting state-, location- and activity-dependent computations (Gasparini & Magee, 2006; Narayanan & Johnston, 2012; Tigerholm *et al.* 2013; Bieri *et al.* 2014; Das & Narayanan, 2014).

The positioning of a neuronal compartment along the integrator–coincidence detector (I–CD) continuum and its encoding strategy are critically determined by its intrinsic properties (Hodgkin, 1948; Hong *et al.* 2007, 2012; Famulare & Fairhall, 2010; Ratté *et al.* 2013; Das & Narayanan, 2014). The spike-triggered average (STA), computed as the average current stimulus that triggers a spike in a neuron injected with Gaussian white noise

current, reflects the exact positioning of a compartment along the I–CD continuum (Ratté *et al.* 2013), with the STA of an integrator (class I excitability) showing no spectral selectivity while that of a coincidence detector (class II/III) showing strong spectral selectivity (Das & Narayanan, 2014). Although the STA allows for the visualization of the coincidence detection capabilities of a neuron and its transition from an integrator to a coincidence detector, this characteristic of the STA has not been harnessed towards quantifying coincidence detection in neurons. In this study, we developed quantitative metrics for the temporal window of integration/coincidence detection based on the structure of the STA. We employed these metrics in conjunction with recently established quantitative measures for spike initiation dynamics (Das & Narayanan, 2014) to assess the emergence and dependence of coincidence detection and STA spectral selectivity on various channel combinations and somatodendritic gradients.

We found that the presence of resonating conductances, either independently or synergistically when expressed together, led to the emergence of spectral selectivity in the spike initiation dynamics and a significant reduction in the temporal window for coincidence detection (class II/III excitability). As a consequence, resonating conductances constructed efficient coincident detectors not just by reducing the width of the spike-proximal positive lobe (SPPL) of the STA but also by enforcing a negative weightage for excitatory inputs that arrive beyond the SPPL. The presence of transient K^+ channels reduced the STA characteristic frequency and broadened the CDW, but persistent Na^+ channels sharpened the CDW by strengthening the spectral selectivity in the spike initiation dynamics. Finally, in a morphologically precise model endowed with experimentally constrained channel gradients, we found that somatodendritic compartments expressed maps of strong theta-frequency selectivity (4–8 Hz) in spike initiation dynamics and gamma-frequency CDW. Based on our results, we

postulate that gradients in active dendritic conductances enable graded gamma frequency coincidence detection in hippocampal pyramidal neurons, with proximal and distal dendritic regions tuned for slow (25–60 Hz) and fast (60–150 Hz) gamma oscillatory inputs, respectively.

Methods

We first employed a single compartmental model to preclude the confounding effects of morphology and analysed the effect of interactions between different subthreshold voltage-gated ion channels (VGICs) on the neuronal spiking dynamics and on the CDW. We performed detailed sensitivity analyses involving all parameters associated with the kinetics of the VGICs to study their individual as well as their combined effects on previously established STA-derived measures and on the CDW. We then moved to a morphologically realistic model with physiologically constrained gradients in dendritic VGICs to study the transition in mode of operation of different dendritic compartments of a CA1 pyramidal neuron and quantified the CDW in the presence of multiple dendritic VGICs interacting with each other. All our models and their parameters were based on the large body of quantitative experimental data available on hippocampal CA1 pyramidal neurons.

The single compartmental model and channel kinetics

A single compartmental model comprising a cylindrical soma of 100 μm length and 100 μm diameter was used with values of the specific membrane resistivity R_m and specific membrane capacitance C_m fixed at 30 kΩ cm^2 and 1 μF cm^{-2}, respectively. Different combinations of VGICs were used to study their interactions and the effects of such interactions on the spectrotemporal selectivity in the spike initiation dynamics and the CDW of the neuronal compartment. Across all VGIC configurations and all analyses presented in this study, the model consisted of fast sodium (NaF) channels and delayed rectifier potassium (KDR) channels, as a prerequisite for generating spikes. Reversal potentials for Na$^+$ and K$^+$ were set to 55 mV and –90 mV, respectively. The voltage dependencies and kinetics for NaF and KDR potassium channels were adopted from experimental measurements on hippocampal pyramidal neurons (Magee & Johnston, 1995; Hoffman *et al.* 1997; Migliore *et al.* 1999). For simulations with hyperpolarization-activated cyclic nucleotide gated (HCN) channels, the kinetics and voltage-dependence properties were adopted from Magee (1998), Poolos *et al.* (2002) and Gasparini *et al.* (2004) and the reversal potential was set to –30 mV. Kinetics of T-type calcium (CaT) channels were adopted from Shah *et al.* (2008) with the current through them modelled based on

the Goldman–Hodgkin–Katz formulations. The default internal and external Ca^{2+} concentrations were fixed at 50 n$_M$ and 2 m$_M$, respectively. The kinetics of potassium (KA) channels were based on Migliore *et al.* (1999), and the model for persistent sodium (NaP) channels was obtained from Uebachs *et al.* (2010).

The morphologically realistic model and channel gradients

A three-dimensional reconstruction of a CA1 pyramidal neuron (*n123*) obtained from NeuroMorpho.Org (Pyapali *et al.* 1998; Ascoli *et al.* 2007) was employed with several constraints placed on it to match its electrophysiological measurements with experimental values (Rathour & Narayanan, 2014). Passive properties were set such that the input resistance (R_{in}) was almost uniform (~120 MΩ) across the somato-apical trunk compartments by adjusting R_m and axial resistivity (R_a) as functions of radial distance of the compartment (x) from the soma (Narayanan & Johnston, 2007):

$$R_m = R_m^{soma} + \left(\frac{R_m^{end} - R_m^{soma}}{1 + \exp\left((300 - x)/50\right)} \right) \quad (1)$$

$$R_a = R_a^{soma} + \left(\frac{R_a^{end} - R_a^{soma}}{1 + \exp\left((300 - x)/50\right)} \right) \quad (2)$$

where $R_m^{soma} = 125$ kΩ cm^2 and $R_a^{soma} = 120$ Ω cm are somatic values and $R_m^{end} = 85$ kΩ cm^2 and $R_a^{end} = 70$ Ω cm are values at the terminal location of the apical trunk (~425 μm for this model). Apical oblique dendrites had the same R_m and R_a values as the point of their origin on the apical trunk. The basal and axonal compartments had the same R_m and R_a values as the soma. C_m was uniformly set to 1 μF cm^{-2}.

The active conductances were distributed across the dendritic arbor in a manner that was consistent with physiological constraints. We first introduced NaF and KDR channels into the model with uniform densities across the somatodendritic arbor with $\overline{g}_{NaF} = 16$ mS cm^{-2} and $\overline{g}_{KDR} = 10$ mS cm^{-2}. The density of the axonal NaF channels at the axon initial segment was five times that at the soma (Fleidervish *et al.* 2010). A somatodendritic HCN channel gradient (Magee, 1998; Lorincz *et al.* 2002) was set as a sigmoidal function (Fig. 7*A*) of the radial distance from soma, x (Narayanan & Johnston, 2007):

$$\overline{g}_h(x) = g_h^{Base} \left(1 + \frac{F_h}{1 + \left(\exp\left((320 - x)/50\right)\right)} \right) \quad (3)$$

g_h^{Base} represents the somatic density of HCN channels, with a default value of 25 μS cm^{-2}, and F_h (= 12) quantifies the fold increase in the density of HCN channels. The half-maximal voltage for activation of HCN channels was

varied along the somatodendritic axis such that it was –82 mV for $x \leq 100 \, \mu$m, increased linearly from –82 mV to –90 mV for $100 > x \geq 300 \, \mu$m and –90 mV for $x > 300 \, \mu$m (Magee, 1998). The T-type calcium (CaT) channel density across the somatodendritic axis was tuned in the following manner (Fig. 7*A*):

$$\bar{g}_{CaT}(x) = g_{CaT}^{Base} \left(1 + \frac{F_{CaT}}{1 + (\exp((350 - x)/50))} \right) \quad (4)$$

g_{CaT}^{Base} ($= 80 \, \mu$S cm^{-2}) represents the somatic density of CaT channels and F_{CaT} ($= 30$) quantifies the fold increase in the density of CaT channels. A linear somatodendritic gradient in density of potassium (KA) channels was set as follows (Fig. 7*A*):

$$\bar{g}_{KA}(x) = g_{KA}^{Base} (1 + F_{KA}x/100) \quad (5)$$

where g_{KA}^{Base}, representing the somatic density of KA channels, was set at 3.1 mS cm^{-2} and F_{KA} ($= 8$) quantifies
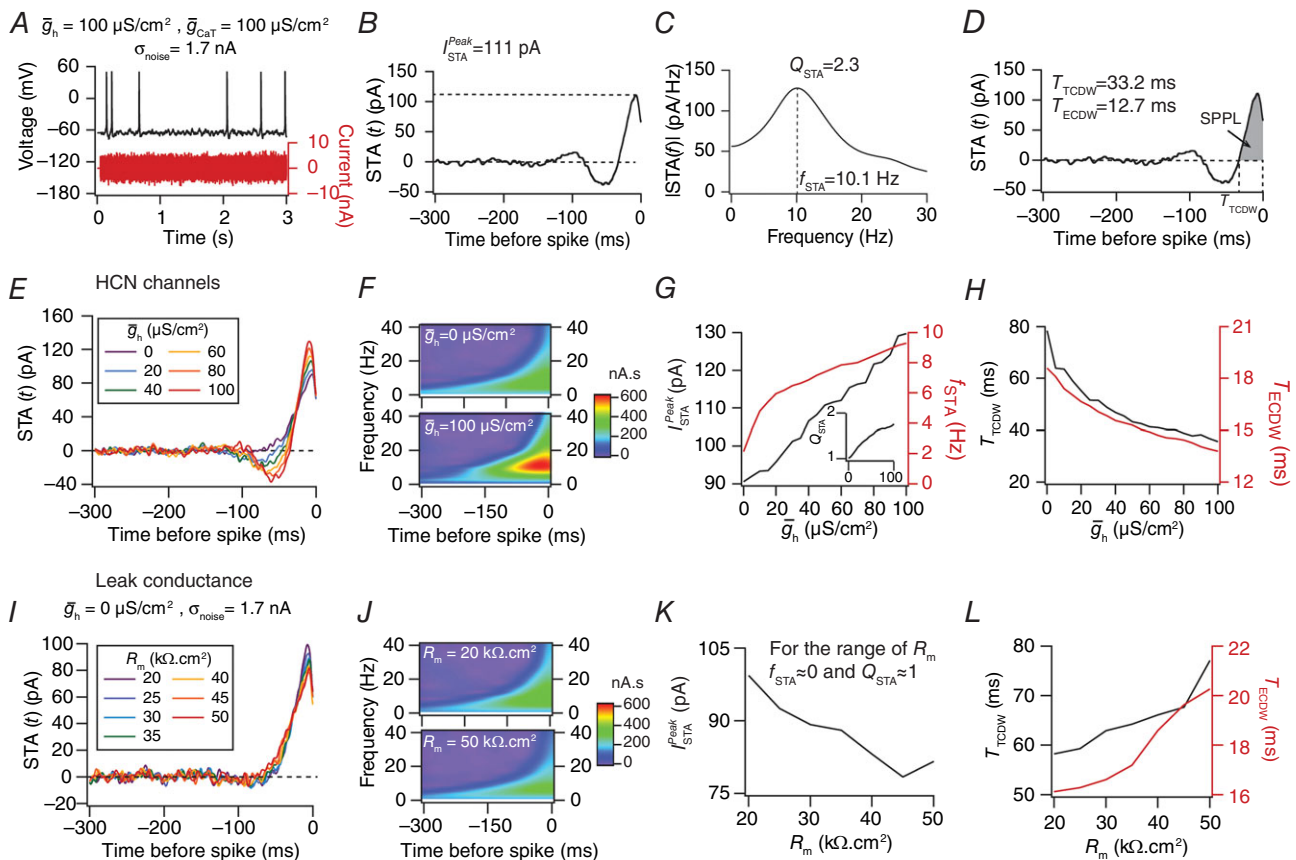

Figure 1. Quantitative measurements derived from the spike-triggered average (STA) revealed differences between HCN and leak conductances in regulating spike initiation dynamics and coincidence detection

A, the STA of a single-compartment neuronal model was measured by injecting zero-mean Gaussian white noise (with standard deviation σ_{noise}) to elicit spikes. The graph represents 3 s of the simulation. *B*, the STA was represented on a negative time axis to depict the average current that resulted in an action potential. I_{STA}^{Peak} represents the peak STA current computed from this temporal representation. *C*, the Fourier transform of the STA revealed its spectral selectivity at a characteristic frequency, f_{STA}, with the strength of selectivity measured as Q_{STA}. *D*, the total CDW (T_{TCDW}) was computed as the temporal distance between the spike and the point of first zero crossing of the STA from the spike. The effective CDW (T_{ECDW}) was measured by weighting the total CDW by the amplitude of the STA within the spike-proximal positive lobe (SPPL, shaded area; see eqn (6)). *E*, STA progressively transformed from class I to class II/III with increasing density of HCN channels, $\bar{g}_h$. *F*, wavelet analysis showed a strong temporally localized theta-frequency selectivity in the presence of HCN channels. *G*, the I_{STA}^{Peak} increased with increase in HCN channel density as did the f_{STA} and Q_{STA} (inset). *H*, the total (T_{TCDW}) and effective (T_{ECDW}) CDWs, computed from traces shown in *E*, decreased with increasing $\bar{g}_h$. *I*, STA traces in the absence of HCN channels in the compartment, shown for various values of R_m. *J*, wavelet analysis revealed absence of theta spectral selectivity for different values of R_m, in the absence of HCN channels. *K*, the I_{STA}^{Peak}, f_{STA} and Q_{STA} ($\sim$1) decreased with increasing R_m, with the values of f_{STA} and Q_{STA}. *L*, the total (T_{TCDW}) and effective (T_{ECDW}) CDWs decreased with increasing R_m. Simulations for results shown in *E–H* were performed with only HCN, NaF and KDR channels expressed in the compartment, while those from *I–L* were performed with only NaF and KDR channels.

the slope of the linear increase in its density. To account for the differences in the properties of the KA channels in the CA1 dendrites, a proximal model with a half-maximal voltage for activation ($V_{1/2}$) of 11 mV and distal model with $V_{1/2}$ of –1 mV were used for proximal and distal dendritic locations, respectively (Hoffman *et al.* 1997; Migliore *et al.* 1999). All gradient parameters were tuned to match critical physiological measurements (Fig. 7*B*) with corresponding experimental findings across the somato-apical trunk (Magee, 1998; Migliore *et al.* 1999; Lorincz *et al.* 2002; Ulrich, 2002; Narayanan & Johnston, 2007; Hu *et al.* 2009; Vaidya & Johnston, 2012).

Computing spike-triggered average and coincidence detection window

The STA and its spectrotemporal features were computed as described previously (Das & Narayanan, 2014). Briefly,

zero-mean Gaussian white noise current with a standard deviation σ_{noise}, adjusted so as to obtain a firing rate of ~1–2 Hz, was injected into the single compartment model to estimate the STA as the average current stimulus that triggers a spike (Fig. 1*A*). While the effect of altering σ_{noise} in a single compartmental model was already assessed (Das & Narayanan, 2014), we investigated the same in the morphologically realistic model to assess the impact of stimulus statistics on the STA and coincidence detection (Fig. 7*H–K*). The peak STA current (I_{STA}^{Peak}) was computed from the temporal representation of the STA (Fig. 1*B*), whereas the STA characteristic frequency (f_{STA}) and strength of frequency selectivity (Q_{STA}, defined as |STA(f_{STA})| divided by |STA(0.5)|), were computed from its Fourier representation (Fig. 1*C*). Wavelet analysis was performed on the STA (Das & Narayanan, 2014) using the complex Morlet wavelet (Grossman & Morlet, 1984) and wavelet coefficients were computed spanning a frequency range of 1–85 Hz (e.g. Fig. 2*C*). Across models and
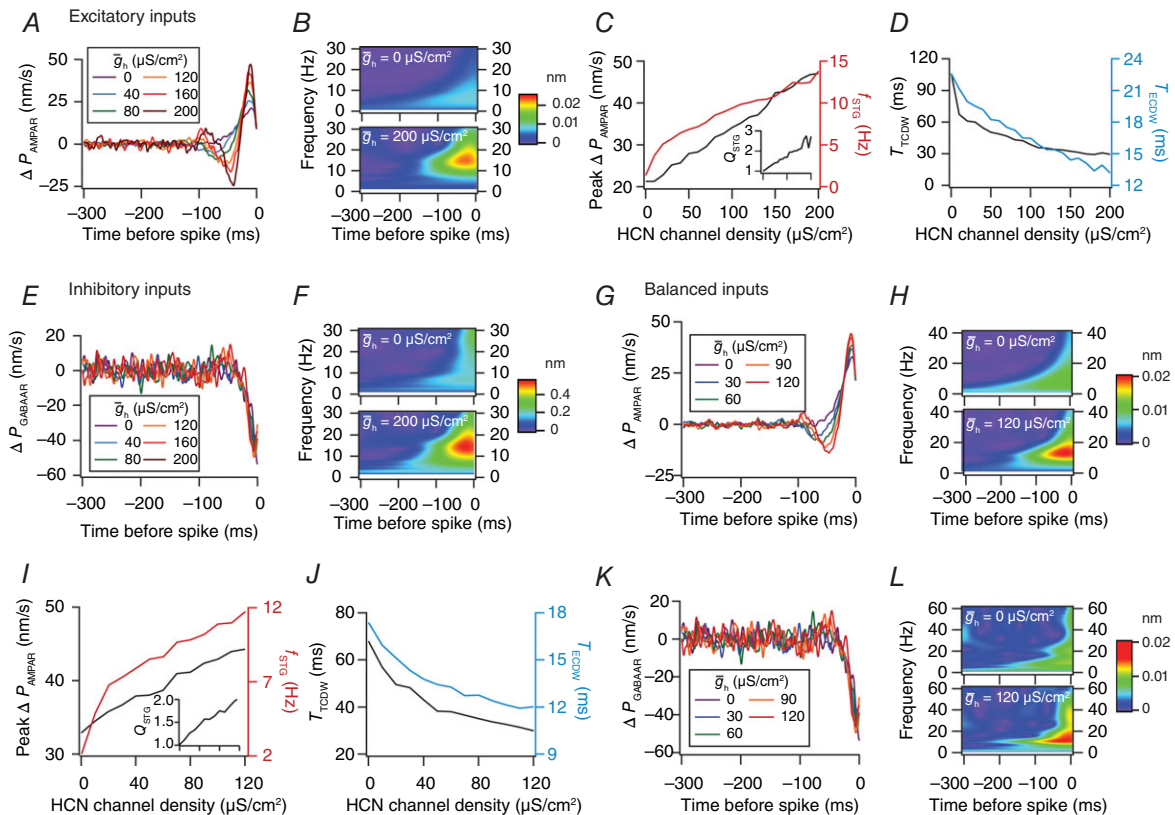

Figure 2. Computation of spike-triggered conductance (STG) revealed theta-frequency selectivity in the presence of HCN channels when conductance was used as input
A–D, AMPAR STG computed in the presence of exclusively excitatory inputs. *A*, AMPAR STG traces depicted for various densities of HCN channels. *B*, wavelet analysis of the STG revealed spectrotemporally localized selectivity in the presence of HCN channels. *C*, the peak change in permeability, frequency selectivity as well as strength of selectivity (inset) increased monotonically with increasing density of HCN channels. *D*, the total and effective CDW decreased with increasing HCN channel density. *E* and *F*, same as *A* and *B* for GABA$_A$R STG computed with exclusively inhibitory inputs. *G–J*, same as *A–D* computed with balanced excitatory–inhibitory inputs. *K* and *L*, same as *E* and *F* computed with balanced excitatory–inhibitory inputs. The fluctuations in GABA$_A$R STGs (panels *E* and *K*) may be noted. $\bar{g}_{Na} = 20$ mS cm^{-2}, $\bar{g}_{KDR} = 0.7$ mS cm^{-2}.

parametric variations, the total time of simulation was adjusted such that no less than 1000 spikes were employed towards computing the STA.

To quantify the integration/coincidence-detection window of the neuronal compartment from the STA, we developed two additional measures, the total CDW (T_{TCDW}) and the effective CDW (T_{ECDW}), which were computed based on the temporal location of first zero crossing (measured from the spike; $t = 0$) of the STA (Fig. 1*D*). T_{TCDW} quantified the entire temporal expanse over which the inputs were positively weighted by the neuron, and was defined as the distance between the spike ($t = 0$ ms on STA(t)), and the temporal location where the STA(t) made its first zero-crossing (Fig. 1*D*). T_{ECDW}, on the other hand, accounted for the difference in weightage of each temporal location within this region of positive integration (the spike-proximal positive lobe, SPPL; shaded region in Fig. 1*D*) and was computed as follows (cf. effective duration in Gabor, 1946):

$$T_{ECDW} = \sqrt{\dfrac{\displaystyle\int_{-T_{TCDW}}^{0} t^2\, STA^2(t)\, dt}{\displaystyle\int_{-T_{TCDW}}^{0} STA^2(t)\, dt}} \quad (6)$$

Computing spike-triggered conductance

In computing the spike-triggered conductance (STG), Goldman–Hodgkin–Katz models for the AMPA and/or GABA$_A$ receptors were inserted into the neuronal compartment. The current through AMPA receptors, as a function of voltage (v) and time (t) was modelled as a sum of currents carried by potassium and sodium ions (Narayanan & Johnston, 2010):

$$I_{AMPAR}(v, t) = I^{Na}_{AMPAR}(v, t) + I^{K}_{AMPAR}(v, t) \quad (7)$$

where

$$I^{Na}_{AMPAR}(v, t) = \overline{P}_{AMPAR}\, P_{Na}\, \frac{vF^2}{RT}$$
$$\left(\frac{[Na^+]_i - [Na^+]_o \exp\left(-\frac{vF}{RT}\right)}{1 - \exp\left(-\frac{vF}{RT}\right)} \right) \quad (8)$$

$$I^{K}_{AMPAR}(v, t) = \overline{P}_{AMPAR}\, P_K\, \frac{vF^2}{RT}$$
$$\left(\frac{[K^+]_i - [K^+]_o \exp\left(-\frac{vF}{RT}\right)}{1 - \exp\left(-\frac{vF}{RT}\right)} \right) \quad (9)$$

$\overline{P}_{AMPAR}$ is the maximum permeability of the AMPA receptor, whose value was modelled as Gaussian

distributed white noise. P_{Na} was taken to be equal to P_K, given experimental observations (Dingledine *et al.* 1999). The internal and external concentrations of sodium and potassium ions were $[Na^+]_i = 18$ mM, $[Na^+]_o = 140$ mM, $[K^+]_i = 140$ mM, $[K^+]_o = 5$ mM, which resulted in reversal potentials of $+55$ mV and -90 mV, respectively.

The current through GABA$_A$ receptors was modelled as in Mishra & Narayanan (2015):

$$I_{GABAAR}(v, t) = \overline{P}_{GABAAR}\, \frac{vF^2}{RT}$$
$$\left(\frac{[Cl^-]_i - [Cl^-]_o \exp\left(-\frac{vF}{RT}\right)}{1 - \exp\left(-\frac{vF}{RT}\right)} \right) \quad (10)$$

where $\overline{P}_{GABAAR}$ is the maximum permeability of the GABA$_A$ receptor, whose value was once again modelled as Gaussian distributed white noise. The internal and external concentrations of chloride ions were fixed at 5 and 98 mM, respectively, which resulted in a reversal potential of -80 mV.

Simulations were performed with either the AMPAR or GABA$_A$R inserted into the single compartment to investigate their individual contribution, following which their combined contribution was assessed. These simulations were performed with NaF, KDR and HCN channels in the single compartmental model (Fig. 2). The change in conductance $\sim$1000 ms preceding a spike was measured and averaged across spikes to obtain the STG (Fig. 2). Analogous STA-derived metrics (I_{STG} as a surrogate for the excitability of the neuron in response to activation of receptor currents; total and effective CDWs; f_{STG} and Q_{STG} measuring the frequency selectivity and strength of frequency selectivity, respectively) were computed from the temporal and the spectral domain representations of the STG.

Assessing coincidence detection of pairs of afferent synaptic inputs

Our model excitatory synapse comprised AMPA receptors, whose excitatory postsynaptic current (EPSC) as a function of voltage (v) and time (t) was modelled as in Narayanan & Johnston (2010):

$$I_{AMPAR}(v, t) = I^{Na}_{AMPAR}(v, t) + I^{K}_{AMPAR}(v, t) \quad (11)$$

where

$$I^{Na}_{AMPAR}(v, t) = \overline{P}_{AMPAR}\, P_{Na}\, s(t)\, \frac{vF^2}{RT}$$
$$\left(\frac{[Na^+]_i - [Na^+]_o \exp(-vF/RT)}{1 - \exp(-vF/RT)} \right) \quad (12)$$

and

$$I_{\mathrm{AMPAR}}^{\mathrm{K}}(\nu, t) = \overline{P}_{\mathrm{AMPAR}} \, P_{\mathrm{K}} \, s(t) \, \frac{\nu F^2}{RT}$$

$$\left(\frac{\left[\mathrm{K}^+\right]_{\mathrm{i}} - \left[\mathrm{K}^+\right]_{\mathrm{o}} \exp\left(-\nu F/RT\right)}{1 - \exp\left(-\nu F/RT\right)} \right) \quad (13)$$

where F is Faraday's constant, R is the gas constant, T is temperature and $\overline{P}_{\mathrm{AMPAR}}$ is the maximum permeability of AMPAR. The additional term $s(t)$ governed the AMPAR kinetics and was set as follows:

$$s(t) = a \left(\exp\left(-t/\tau_{\mathrm{d}}\right) - \exp\left(-t/\tau_{\mathrm{r}}\right) \right) \quad (14)$$

where a normalized $s(t)$ such that $0 \leq s(t) \leq 1$, τ_{d} ($= 10$ ms) represents the decay time constant and τ_{r} ($= 2$ ms) represents the rise time. P_{Na} was equal to P_{K}. Internal and external ionic concentrations were set as before: $[\mathrm{Na}^+]_{\mathrm{i}} = 18$ mM, $[\mathrm{Na}^+]_{\mathrm{o}} = 140$ mM, $[\mathrm{K}^+]_{\mathrm{i}} = 140$ mM, $[\mathrm{K}^+]_{\mathrm{o}} = 5$ mM, which established the reversal potentials for sodium and potassium ions at $+55$ mV and -90 mV, respectively. We confirmed the reversal potential for AMPAR as ~ 0 mV. Pairs of AMPAR EPSCs were injected at different locations along the somatodendritic trunk with varying inter-pulse intervals (IPIs). The resulting somatic EPSPs were recorded for IPI values ranging from 10 to 100 ms, and for different values of synaptic strength determined by the value of $\overline{P}_{\mathrm{AMPAR}}$. Coincidence detection was said to occur when a single somatic action potential was generated upon the joint occurrence of the first and the second EPSPs. Cases where the permeability of the AMPAR was such that the first EPSP alone was sufficient to elicit a somatic action potential or where neither of the two EPSCs elicited action potentials were considered invalid for our analysis. To determine the extent of the coincidence detection window at each somatodendritic compartment, we determined the largest IPI (IPI$_{\mathrm{max}}$) for which coincidence detection occurred for inputs at that compartment, by presenting EPSCs whose IPIs ranged from 100 to 10 ms in steps of 1 ms. As a higher input strength was required to elicit somatic action potentials for distal dendritic inputs, this procedure was repeated for several values of $\overline{P}_{\mathrm{AMPAR}}$ at each location. For each value of $\overline{P}_{\mathrm{AMPAR}}$, IPI$_{\mathrm{max}}$ was plotted as a function of the distance (from the soma) of the compartment where the two EPSCs were injected. For the passive morphology case, we tested with IPIs ranging from 400 ms to 100 ms since the neuron exhibited large integration windows.

Computational details

The input resistance, R_{in}, of a neuronal compartment was computed by measuring the steady-state voltage response to current pulses of -50 to 50 pA in steps of 10 pA for 500 ms each. The steady-state voltage response was then plotted against the current amplitude and the slope of this linear relationship constituted R_{in} of that compartment. The local resonance frequency, f_{R}, was computed by locally injecting a chirp stimulus spanning 25 Hz in 25 s and the frequency at which the impedance amplitude profile (ZAP) of the compartment reached its maximum was designated as f_{R} of the neuronal compartment (Narayanan & Johnston, 2007). The transfer resonance frequency (f_{TR}) was computed by placing the chirp input at different locations along the dendrite and measuring the voltage response at the soma. The frequency at which the transfer ZAP reached its maximum was defined as f_{TR} (Hu *et al.* 2009; Vaidya & Johnston, 2013; Das & Narayanan, 2014).

The NEURON simulation environment was employed for modelling and all analyses were performed using the custom-built software written in Igor Pro (Wave-Metrics Inc., Lake Oswego, OR, USA). All simulations were performed at 34°C, accounting for all the Q_{10} values for each channel and their kinetics, with an integration time step of 25 μs. The default resting potential was fixed at -65 mV, and simulations were repeated at several repeated resting potentials to assess the impact of different conductances active at different voltages.

Results

Measurements for quantifying the integration/ coincidence detection window from the STA

We first employed a single-compartmental conductance-based model to understand the kinetic interactions between the different co-expressing channels, before progressing to a morphologically precise model with multiple ion channel gradients to analyse the spatio-kinetic interactions among these channels. Specifically, we assessed the interactions between six different VGICs (NaF, KDR, HCN, KA, CaT, NaP), which are known to co-express in CA1 pyramidal neurons in various different combinations, to understand their roles in spike initiation dynamics and coincidence detection. In doing this, we employed previously established (Das & Narayanan, 2014) quantitative measures for understanding the STA and its spectral selectivity (Fig. 1), namely the peak STA current ($I_{\mathrm{STA}}^{\mathrm{Peak}}$), the STA characteristic frequency (f_{STA}) and the strength of STA spectral selectivity (Q_{STA}).

Additionally, although the shape of the STA provides insights into the integration/coincidence detection abilities of the underlying neuronal compartment (Ratté *et al.* 2013; Das & Narayanan, 2014), this feature of the STA has not been exploited in quantifying the window for integration/coincidence detection. To fill this gap, we reasoned that the spike-proximal positive lobe

(SPPL; shaded area in Fig. 1*D*) of the STA constitutes the temporal domain over which integration/coincidence detection of excitatory inputs would occur; the shorter this temporal domain, the more stringent the window for integration/coincidence detection. Our first measure of CDW (T_{TCDW}) was therefore defined as the temporal extent of the SPPL. Although the temporal extent provides a window for coincidence detection, it was clear from the shape of the STA that the weightage for inputs arriving at each temporal location within this window in eliciting a spike was variable (Fig. 1*D*). We exploited this feature of the STA in defining an effective CDW (T_{ECDW}), which was a STA-weighted measure of the SPPL (eqn (6)). Although this measure follows the 'effective duration' metric defined by Gabor for any arbitrary signal (Gabor, 1946), we computed this effective duration only over the SPPL (Fig. 1*D*) to define T_{ECDW}. We noted from these definitions that T_{ECDW} would equal T_{TCDW} when STA(t) was uniformly weighted across the entire SPPL. While these measurements quantifying the SPPL of the STA could be used to assess the integration time window in neurons with class I excitability, it is an efficacious measure for the CDW for those endowed with class II/III excitability.

The presence of HCN channels imparted coincidence detector properties to the neuron

Although the impact of the presence of HCN channels on the STA measurements are established (Das & Narayanan, 2014), their impact on the CDW was unknown. We inserted HCN conductance with various densities into our single compartmental model that was endowed with the spike-generating conductances NaF and KDR, and computed the STA to measure both the total and the effective CDW of the compartment. We first confirmed that the STA was class II with a strong theta-frequency selectivity and the I_{STA}^{Peak}, f_{STA} and Q_{STA} increased with increasing density of HCN channels (Fig. 1*E–G*). Next we computed the T_{TCDW} and T_{ECDW} and found both to decrease with increase in HCN conductance density, with ranges of T_{ECDW} falling in the gamma frequency range (Fig. 1*H*). This implied that the CDW became narrow with higher expression of HCN channels, and is consistent with the literature that an increase in HCN channels reduces temporal summation (Magee, 1998, 1999; Remme & Rinzel, 2011).

Resonating conductances construct efficient coincident detectors by enforcing a negative weightage for excitatory inputs beyond the coincidence detection window

Was graded constriction in the CDW unique to graded increases in the HCN channel conductance? Could

these changes be achieved through increases in the leak conductance? To address these questions, we removed HCN channels from the model and varied the leak conductance density by altering R_m. We found that the STA exhibited class I features with no spectral selectivity as evinced from both the wavelet and Fourier analysis, although I_{STA}^{Peak} increased with increase in R_m reflective of an increase in excitability (Fig. 1*I–K*). Despite the absence of class II features, increase in R_m resulted in a broadening of the SPPL of the STA, bringing about an increase in the T_{TCDW} and T_{ECDW} (Fig. 1*L*). These results suggest that in the absence of a resonating conductance, changes in leak conductance ($g_{leak} = 1/R_m$) could alter the integration time window in a class I STA, but without switching to the class II regime.

If altering passive properties (R_m and C_m; Tables 1 and 2, Fig. 1*I–K*) could regulate the CDW, what is the need for a resonating conductance? What additional impact do resonating conductances have on coincidence of excitatory afferent inputs? In answering this we noted that, in the absence of resonating conductances, the STA continues to remain largely class I, with significantly small negative lobes beyond the SPPL (Fig. 1*I*). However, upon a progressive increase in density of resonating conductances, not only does the width of the SPPL incrementally decrease, but also a gradually larger negative lobe emerges at a temporal location beyond the SPPL (class II/III STA, Fig. 1*E*; also see analyses with CaT channels, below). Whereas the former implies that the window for integration of excitatory inputs has shrunk, the latter translates to a negative weightage to excitatory inputs that arrive beyond the SPPL (Meng *et al.* 2012; Ratté *et al.* 2013; Das & Narayanan, 2014). Therefore, for eliciting a spike in neurons endowed with resonating conductances, not only do inputs have to arrive within a restricted time window, but they will be significantly negatively weighted if they come beyond that time window (cf. the negative lobe in the EPSP decay waveform introduced by HCN channels (Magee, 1998; Poolos *et al.* 2002) and synchrony transfer in class II/III membranes (Hong *et al.* 2012; Ratté *et al.* 2013). Together, these results emphasize the need for the presence of resonating conductances in effectuating strong theta-frequency selectivity in the STA and sharp gamma-range coincidence detection. It should be noted that negative lobes in the hippocampal pyramidal STA could be achieved by changing the after-hyperpolarization conductances and/or by altering stimulus statistics (Prescott *et al.* 2006, 2008*b*; Prescott & Sejnowski, 2008; Higgs & Spain, 2009; Famulare & Fairhall, 2010; Kispersky *et al.* 2012; Mease *et al.* 2013; Ratté *et al.* 2013; Das & Narayanan, 2014). However, quantification of the associated STA revealed its spectral selectivity to be weak and in the delta-frequency range (Das & Narayanan, 2014), implying a smaller negative lobe than what could be achieved by the additional presence of resonating conductances.

Table 1. Sensitivity analysis for STA and CDW measurements in a single compartmental model corresponding to parameters associated with T-type calcium channels

Parameters	Tested range	I_{STA}^{Peak}	f_{STA}	Q_{STA}	T_{TCDW}	T_{ECDW}
C_m (μF cm^{-2})	0.5–1	Decreased	Decreased	Decreased*	Increased	Increased
R_m (Ω cm^2)	20–40	Decreased	Decreased	Decreased*	Increased	Increased
V_m (mV)	−67 to −60	U-shaped	Bell-shaped	Bell-shaped*	U-shaped	U-shaped
$\bar{g}_{CaT}$ (μS cm^{-2})	0–200	Decreased	Increased	Increased	Decreased	Decreased
$V_{1/2,act}$ (mV)	−70 to −50	U-shaped	Decreased	Decreased	Increased	Increased
$V_{1/2,inact}$ (mV)	−95 to −75	Decreased	Increased	Increased	Decreased	Decreased*
τ_{act} (ms)	1–5	No change	Decreased	Decreased	Increased	Increased
τ_{inact} (ms)	1–160	Decreased	Asymmetric bell-shaped	Asymmetric bell-shaped	U-shaped*	U-shaped*
$\bar{g}_{Na}$ (mS cm^{-2})	15–29	Decreased	Increased	Increased	Decreased	Decreased
$\bar{g}_{KDR}$ (mS cm^{-2})	1–40	Increased	Increased	Decreased	No change	Decreased*
$\bar{g}_{CaT}$ (μS cm^{-2}) (without activation gate)	0–70	Increased	Increased	Increased	Decreased	Decreased

These simulations were performed in the presence of CaT, NaF and KDR channels. Changes in the STA-derived measures are with respect to increase in parameter values. Increases in the voltages (V_m and $V_{1/2}$) indicate shifts towards more depolarized potentials. Also see Fig. 2. Default $\bar{g}_{CaT} = 10\ \mu$S cm^{-2}. *Small (<10%) change.

Table 2. Sensitivity analysis for STA and CDW measurements in a single compartmental model when T-type calcium channels and HCN channels were co-expressed

Parameters	Tested range	I_{STA}^{Peak}	f_{STA}	Q_{STA}	T_{TCDW}	T_{ECDW}
$\bar{g}_{CaT}$ (μS cm^{-2})	0–200	Decreased	Increased	Increased	Decreased	Decreased
$\bar{g}_h$ (μS cm^{-2})	0–200	Increased	Increased	Increased	Decreased	Decreased
$V_{1/2,act}$ CaT (mV)	−70 to −50	Increased	Decreased	Decreased	Increased	Increased
$V_{1/2,inact}$ CaT (mV)	−95 to −75	Decreased	Increased	Increased	Decreased	Decreased
τ_{act} CaT (ms)	1–5	Increased	Decreased	Decreased	Increased	Increased
τ_{inact} CaT (ms)	1–160	Decreased	Asymmetric bell-shaped	Asymmetric bell-shaped	Increased	Increased
$V_{1/2,act}$ HCN (mV)	−120 to 0	Sigmoidal increase	Bell-shaped	Bell-shaped	U-shaped	U-shaped
τ_{act} HCN (ms)	3.3–191.9	Decreased	Asymmetric bell-shaped	Asymmetric bell-shaped	U-shaped*	U-shaped*

These simulations were performed in the presence of CaT, HCN, NaF and KDR channels. Changes in the STA-derived measures are with respect to increase in parameter values. Increases in the voltages (V_m and $V_{1/2}$) indicate shifts towards more depolarized potentials. Default $\bar{g}_{CaT} = 100\ \mu$S cm^{-2}; $\bar{g}_h = 100\ \mu$S cm^{-2}. Also see Fig. 4. *Small (<10%) change.

Against this we noted that our definitions of integration/coincidence. detection windows were only from the SPPL, without accounting for the negative lobe that acts to further suppress depolarizing inputs arriving at temporal locations beyond the SPPL, and constituted a limitation of our CDW definitions.

The presence of HCN channels imparted theta-frequency spectral selectivity to the spike-triggered conductances

Our investigation of spike initiation dynamics thus far was limited to the use of noise current injection into the neuron. However, as the primary input to neurons is through ligand-gated receptors, it was imperative that spike initiation dynamics were assessed with white noise conductance as input instead of current. This is essential because a simple current injection would not account for voltage-dependent changes in driving force for currents through synaptic receptors. We computed the spike-triggered conductance (STG) by injecting either an AMPAR or a GABA$_A$R white noise conductance, to delineate the individual contributions of excitatory and inhibitory inputs. We found that spike-triggered changes in AMPAR permeability showed a progressively class II/III structure with increase in the density of the HCN channels (Fig. 2A). Consistent with our results on the

STA, the wavelet transform of the STG revealed spectral selectivity in the theta-frequency range in the presence of HCN channels but lacked spectral selectivity in their absence (Fig. 2*B* and *C*). Further, the peak change in permeability (analogous to I_{STA}^{Peak}) monotonically increased with increasing HCN channel density, as did the frequency (f_{STG}; analogous to f_{STA}) and strength (Q_{STG}, analogous to Q_{STA}) of the selectivity (Fig. 2*C*). The total and effective CDWs computed from the STGs also showed a monotonic decrease with increase in the HCN channel density (Fig. 2*D*). Similar results were observed when GABA$_A$ receptors were employed instead of AMPA receptors, with the major change in the sign of the STG (Fig. 2*E*). Although theta-frequency spectral selectivity in GABA$_A$R STG emerged in the presence of HCN channels (Fig. 2*F*), we did not quantitatively analyse these STGs because of fluctuations consequent to the low driving force for GABA$_A$ receptors.

Next, independent Gaussian white noise stimuli were injected through both AMPA and GABA$_A$ receptors, with the standard deviation of their permeabilities adjusted to maintain the membrane resting potential at –65 mV. Given the differences in driving force amplitudes (65 mV for AMPARs and 15 mV for GABA$_A$Rs), the inhibitory standard deviation was higher than that for excitatory inputs (Rudolph *et al.* 2007; Destexhe, 2010). We confirmed that the insertion of HCN channels into the neuronal model receiving such balanced excitatory–inhibitory afferent inputs resulted in theta-frequency spectral selectivity emerging in the STGs associated with the AMPAR and the GABA$_A$R permeabilities. Furthermore, previously observed (Fig. 2*A–H*) monotonic relationships between HCN channel density and all AMPAR STG measurements extended to the case with the balanced excitatory–inhibitory input regime as well (Fig. 2*E–L*). The huge fluctuations in GABA$_A$R STGs, their inverted sign (Fig. 2*K*; cf. Fig. 2*G*) and the emergence of theta-frequency spectral selectivity in the presence of HCN channels (Fig. 2*F*) may also be noted. Together these results suggested that spike-triggered conductances exhibited theta-frequency spectral selectivity in the presence of HCN channels.

Independent presence of CaT channels mediated weak delta-frequency selectivity and strong theta-frequency selectivity upon removal of their activation gate

The independent expression of CaT channels on neuronal membrane is sufficient to sustain intrinsic membrane potential oscillations and membrane resonance, and therefore they are critical regulators of spatiotemporal

integration in neurons (Hutcheon *et al.* 1994; Hutcheon & Yarom, 2000; Perez-Reyes, 2003; Rathour & Narayanan, 2012*a*). What role does this inactivating resonating conductance play in sculpting the spike initiation dynamics and the CDW of a neuron? To answer this, we computed the STA from our model endowed with different densities of the CaT channels. Consistent with their role as resonating conductances that can mediate post-inhibitory rebound, we found that the STA in the presence of CaT channels displayed a prominent negative lobe (Fig. 3*A*). These class II/III characteristics of the STA (Ratté *et al.* 2013; Das & Narayanan, 2014) also translated to a weak delta-frequency (0.5–4 Hz) band-pass spectral structure in the STA, especially for higher densities of CaT channels (Fig. 3*B* and *C*).

Whereas the insertion of HCN channels introduced strong theta-frequency selectivity in the spike initiation dynamics (Fig. 1; Das & Narayanan, 2014), the insertion of CaT channels even at higher densities yielded only weak delta-frequency selectivity. What specific characteristic of these resonating conductances (HCN and CaT) mediated these differences in STA spectral selectivity? The key differences in their physiology are that HCN channels are hyperpolarization-activated and non-inactivating whereas CaT channels are depolarization-activated and inactivating (Hutcheon & Yarom, 2000; Perez-Reyes, 2003; Shah, 2014) and result in important differences in how these channels regulate the impedance phase profile (Rathour & Narayanan, 2012*a*). As resonance in CaT channels is consequent to its inactivation kinetics (Hutcheon *et al.* 1994; Hutcheon & Yarom, 2000; Rathour & Narayanan, 2012*a*), we repeated our simulations after the removal of the activation gate in the Hodgkin–Huxley model of the CaT channels. The presence of only the inactivation gate in the CaT channels, which opened on hyperpolarization and closed on depolarization, rendered these channels to be physiologically similar to HCN channels except for the reversal potential, which would be more depolarized as this is a calcium channel. Consequently, all STA-based measures with the inactivation-only CaT channels exhibited trends similar to those with the independent presence of HCN channels (Das & Narayanan, 2014). Specifically, the STA in the presence of CaT channels lacking their activation gate displayed a prominent class II structure (Fig. 3*D*), with a strong theta-frequency selectivity (Fig. 3*E*) temporally localized to ~100 ms prior to spiking (Fig. 3*F*). I_{STA}^{Peak} decreased with an increase in the density of native CaT channels, but increased with that of inactivation-only CaT channels, consistent with a reduction in model excitability with increase in the inactivation-only CaT channel density (Rathour & Narayanan, 2012*a*) (Fig. 3*G*). Fourier analysis of the STA revealed monotonic increases in f_{STA} and Q_{STA} with increase in channel density for

both native and inactivation-only CaT channels, but the selectivity was strong and transitioned to the theta range of frequencies for the inactivation-only case (Fig. 3H). Both the total and effective CDWs monotonically decreased (Fig. 3I and J) with increasing densities of both channels. In summary, our results showed that CaT channels could mediate weak delta-frequency selectivity in spike initiation dynamics, and the removal of its activation gate resulted in the development of a strong, temporally localized theta-frequency selectivity in the spike initiation dynamics.

CaT channels interacted synergistically with HCN channels to narrow the CDW and increase the frequency and the strength of STA spectral selectivity

Our analyses with the independent presence of HCN/CaT channels demonstrated their critical role in regulating STA and CDW. Neuronal physiology, however, emerges as a consequence of intricate synergistic interactions among several co-expressing VGICs that have overlapping expression and voltage-dependence profiles (Hodgkin & Huxley, 1952; Marder & Goaillard, 2006; Rathour
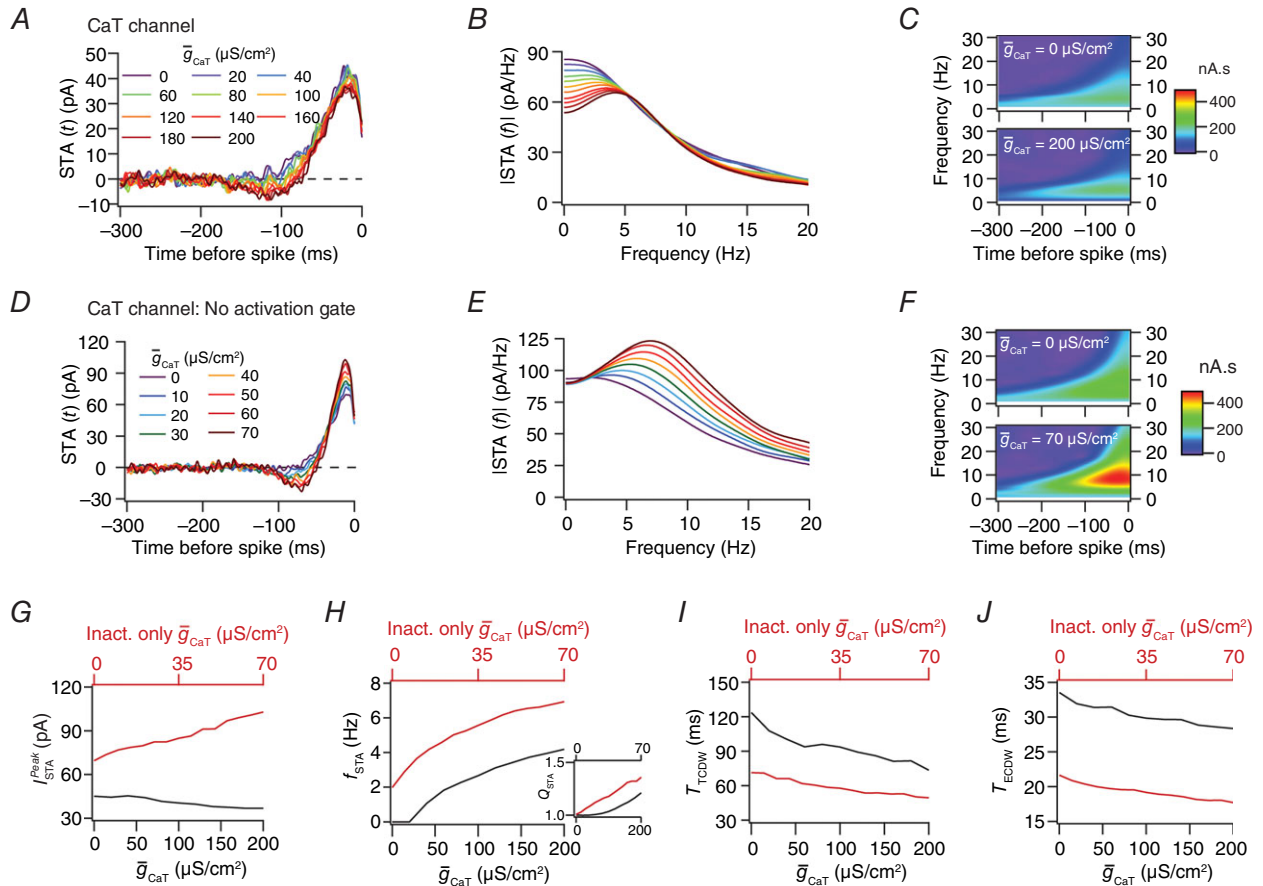

Figure 3. The presence of CaT channels introduced weak delta-frequency selectivity in spike initiation dynamics and strong theta-frequency selectivity when the activation gate was removed

A, STA progressively transformed from class I to class II/III with increasing density of CaT channels, $\bar{g}_{CaT}$ (note the increase in the negative lobe of the STA with increasing $\bar{g}_{CaT}$). *B*, the Fourier transform of the STA at various $\bar{g}_{CaT}$ revealed its band-pass characteristics at higher densities. *C*, wavelet transform of STA in the absence (top) and presence (bottom) of CaT channels. *D*, STA plotted for various values of $\bar{g}_{CaT}$ when the activation gate of the CaT channels was removed. *E*, in the absence of the activation gate, the Fourier transform of the STA at various $\bar{g}_{CaT}$ revealed its theta-frequency band-pass characteristics at higher values of $\bar{g}_{CaT}$. *F*, wavelet analysis revealed a strong, spectrotemporally localized selectivity in the theta-frequency range when CaT channels without the activation gate were introduced. *G*, I_{STA}^{Peak} decreased in the presence of increasing densities of CaT channels, but increased with increasing density of inactivation (Inact.)-only CaT channels, reminiscent of the effect of HCN channels. *H*, f_{STA} and Q_{STA} increased with increase in $\bar{g}_{CaT}$ for both cases, but the frequency selectivity was in the theta range for the Inact. only case. *I* and *J*, the total (T_{TCDW}) and effective (T_{ECDW}) CDWs decreased with increasing $\bar{g}_{CaT}$ but the values were lower for the Inact. only case. $\bar{g}_{Na} = 18$ mS cm^{-2}, $\bar{g}_{KDR} = 0.5$ mS cm^{-2} and $\sigma_{noise} = 1$ nA for simulations with native CaT channels; $\bar{g}_{Na} = 18$ mS cm^{-2}, $\bar{g}_{KDR} = 0.7$ mS cm^{-2} and $\sigma_{noise} = 1.45$ nA for simulations with Inact. only CaT channels. Sensitivity analyses with various model parameters in the presence of CaT channels are presented in Table 1.

& Narayanan, 2012*a*, 2014). Therefore, we turned to analysing the impact of pair-wise co-expression of HCN channels with three subthreshold-activated channels (CaT, KA, NaP), which are known to share subcellular compartments and voltage-dependent profiles with HCN channels (Magee & Johnston, 1995; Hoffman *et al.* 1997; Magee, 1998; Lorincz *et al.* 2002; Vervaeke *et al.* 2006; Nusser, 2009; Lorincz & Nusser, 2010; Kerti *et al.* 2012) in regulating STA and CDW. The spike-generating NaF–KDR channels were present across all channel configurations.

When we incorporated both CaT and HCN conductances together, the STA displayed class II/III characteristics owing to the joint presence of two resonating conductances (Fig. 4*A*), which also reflected as a band-pass structure in the Fourier (Fig. 4*B*) and the spectrotemporal domains (Fig. 4*C*). The dependencies of I_{STA}^{Peak} (Fig. 4*D*), f_{STA} (Fig. 4*E*) and Q_{STA} (Fig. 4*F*) on the CaT conductance in the presence of HCN channels were qualitatively similar to the case where HCN channels were absent (Fig. 2*D* and *E*). However, quantitatively, in the joint
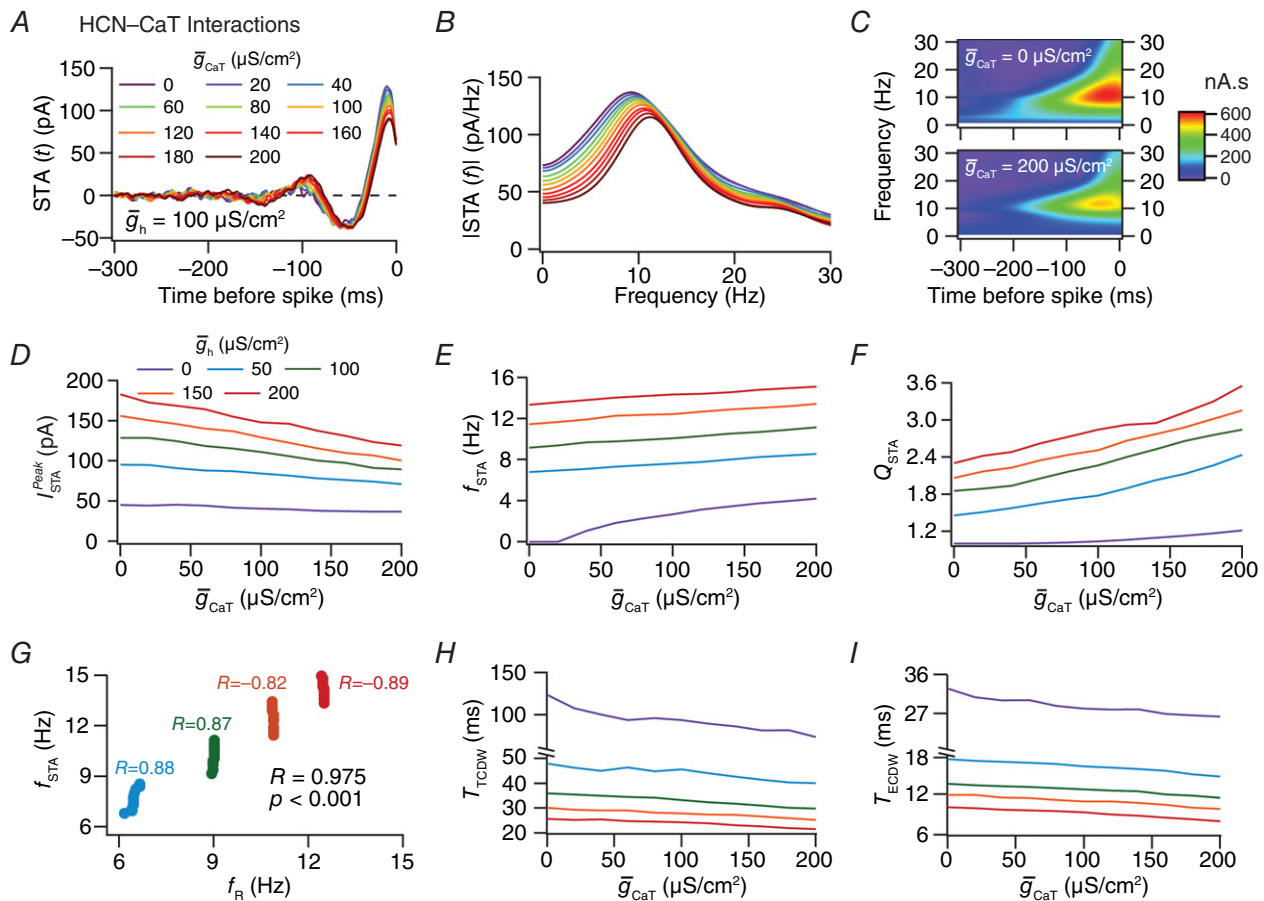

Figure 4. CaT and HCN channels interacted synergistically to regulate STA spectral selectivity and coincidence detection window
A, the STA was class II/III in the presence of two subthreshold resonating conductances (HCN and CaT). *B*, the band-pass nature of the STA was strengthened with increasing density of CaT channels. *C*, wavelet analysis of the STA revealed sharpening of the spectrotemporal localization of theta-frequency selectivity with higher density of CaT channels. *D*, I_{STA}^{Peak} decreased with increasing density of CaT channels and increased with increase in the density of HCN channels. The labels specified in *D* hold for panels *D–I*. *E*, the increase in f_{STA} with increase in density of CaT channels was diminished in the presence of higher HCN channel density. *F*, Q_{STA} increased with increasing density of CaT channels and this increase was aided by the presence of high HCN channel density. *G*, correlation between impedance-based resonance frequency (f_R) and STA characteristic frequency (f_{STA}) plotted for various values of $\bar{g}_{CaT}$ and $\bar{g}_h$. The individual *R* values correspond to Pearson's correlation coefficient for the f_R *vs.* f_{STA} plot computed for a set value of $\bar{g}_h$ across different values of $\bar{g}_{CaT}$. The total *R* value corresponds to Pearson's correlation coefficient computed for the f_R *vs.* f_{STA} plot across all values of $\bar{g}_h$ and $\bar{g}_{CaT}$. *H* and *I*, the total (T_{TCDW}; *H*) and effective (T_{ECDW}; *I*) CDWs decreased with increasing densities of both HCN channels and CaT channels. $\bar{g}_{Na} = 18$ mS cm^{-2}, $\bar{g}_{KDR} = 0.5$ mS cm^{-2} and $\sigma_{noise} = 1.7$ nA. Detailed sensitivity analyses with various parameters associated with both HCN and CaT channels are presented in Table 2.

Table 3. Sensitivity analysis for STA and CDW measurements in a single compartmental model corresponding to parameters associated with potassium channels

Parameters	Tested range	I_{STA}^{Peak}	f_{STA}	Q_{STA}	T_{TCDW}	T_{ECDW}
C_m (μF cm^{-2})	0.5–1	Decreased	Decreased	Decreased[#]	Increased	Increased
R_m (Ω cm^2)	20–40	Decreased	Decreased	Decreased[#]	Increased	Increased
V_m (mV)	−67 to −60	U-shaped	Bell-shaped	Bell-shaped[#]	U-shaped	U-shaped
$\bar{g}_{KA}$ (μS cm^{-2})	0–10	Increased	Decreased (~4 to 1.5)	Decreased[#]	Increased	Increased
$V_{1/2,act}$ (mV)	−5 to 30	Decreased	No change	No change	Decreased	Decreased[*]
$V_{1/2,inact}$ (mV)	−120 to 0	Increased	Decreased	Decreased	Increased	Increased[*]
τ_{act} CaT (ms)	0.03–1.5	Decreased[*]	Increased[*]	Increased[*]	No change	No change
τ_{inact} CaT (ms)	2–100	Decreased[*]	Decreased[*]	Decreased[*]	Increased	Increased
$\bar{g}_{Na}$ (μS cm^{-2})	18–32	Decreased	Increased	Increased[#]	Decreased	Decreased
$\bar{g}_{KDR}$ (μS cm^{-2})	1–15	Increased	Increased	Increased[#]	Decreased[*]	Decreased[*]

These simulations were performed in the presence of KA, NaF and KDR channels. Changes in the STA-derived measures are with respect to increase in parameter values. Increases in the voltages (V_m and $V_{1/2}$) indicate shifts towards more depolarized potentials. Default $\bar{g}_{KA}$ = 5 mS cm^{-2}. Also see Fig. 6 for the cases where $\bar{g}_h$ = 0 mS cm^{-2}. [*]Small (<10%) change. [#]Values are ~1.

presence of HCN and CaT channels, the f_{STA} switched to higher frequencies (Fig. 4*E*) with an enhanced strength of selectivity (Fig. 4*F*) and both CDW measurements reduced beyond the decrease elicited by the independent presence of HCN/CaT channels, with T_{ECDW} reaching the fast gamma/epsilon (Buzsaki, 2006; Freeman, 2007; Colgin & Moser, 2010) frequency band (Fig. 4*H–I*). We also noted that the relationship between the impedance-based resonance frequency (f_R) and f_{STA} (both computed with the same model parameters) exhibited complex dependence on specific conductance values. Additionally, with increase in CaT conductance density, changes in f_{STA} were larger compared to changes in f_R (Fig. 4*G*).

KA channels interacted with HCN channels to reduce the STA characteristic frequency and to broaden the coincidence detection window

KA channels are critical regulators of neuronal excitability, with important roles in regulating action potential properties and propagation, and in modulating sub-threshold response dynamics (Hoffman *et al.* 1997; Kim *et al.* 2005; Rathour & Narayanan, 2012*a*, 2014). How does this inactivating restorative conductance alter the STA and CDW in the absence and the presence of HCN channels? To address this, we first inserted KA channels independently into our model and found that they altered the CDW, and modulated the STA and its weak delta-frequency selectivity that is mediated by the spike-generating conductances (Das & Narayanan, 2014). Specifically, the insertion of KA channels increased I_{STA}^{Peak}, decreased f_{STA} and Q_{STA}, and marginally increased T_{TCDW} and T_{ECDW} (Table 3; Fig. 5, plots with $\bar{g}_h$ = 0 mS cm^{-2}). Upon additional insertion of HCN channels we found that these effects were consistent, but the STA modulation was with reference to the strong theta-frequency selectivity mediated by HCN

channels. Specifically, increase in KA conductance density broadened the SPPL of the STA (Fig. 5*A*), which translated to a reduction in frequency of selectivity (Fig. 5*B*) and an increase in the spectrotemporal spread (Fig. 5*C*) of the STA. Furthermore, increase in KA conductance in the presence of HCN channels increased the I_{STA}^{Peak} (Fig. 5*D*) as expected from a restorative conductance, decreased f_{STA} (Fig. 5*E*) and Q_{STA} (Fig. 5*F*), and marginally increased T_{TCDW} (Fig. 5*H*) and T_{ECDW} (Fig. 5*I*). We also noted that the relationship between the impedance-based resonance frequency (f_R) and f_{STA} (both computed with the same model parameters) exhibited an inverse correlation with changes exclusively in KA channel density (Fig. 5*G*). This inverse correlation is a direct consequence of a differential impact of KA channels on f_R and f_{STA}; an increase in KA conductance increases f_R (Rathour & Narayanan, 2012*a*) but reduces f_{STA} (Fig. 5*E*).

NaP channels sharpened the coincidence detection window and strengthened the frequency selectivity of spike initiation dynamics

We next turned our attention to the NaP channels, which are important regulators of neuronal excitability and temporal summation in several neuronal subtypes, including the hippocampal CA1 pyramidal neurons (French *et al.* 1990; Crill, 1996; Andreasen & Lambert, 1999; Astman *et al.* 2006; Vervaeke *et al.* 2006; Royeck *et al.* 2008). NaP channels are regenerative conductances that are known to amplify subthreshold resonance and facilitate intrinsic oscillations when co-expressed with resonating conductances (Hutcheon *et al.* 1994, 1996; Hu *et al.* 2002; Boehlen *et al.* 2013). We found that the independent presence of NaP channels altered the CDW and modulated the STA and its weak delta-frequency selectivity that is mediated by the spike-generating

conductances (Das & Narayanan, 2014). Specifically, the insertion of NaP channels did not alter f_{STA}, but decreased I_{STA}^{Peak}, marginally increased Q_{STA} and increased T_{TCDW} and T_{ECDW} (Table 5; Fig. 6, plots with $\bar{g}_h = 0$ mS cm^{-2}). These effects of NaP channels on STA and CDW were significantly altered by the additional presence of HCN channels, and the modulation by NaP channels was with reference to the strong theta-frequency selectivity mediated by HCN channels. Specifically, an increase in

NaP conductance density in the presence of HCN channels resulted in a marginal increase in f_{STA} (Fig. 6B–E), a reduction in the spectrotemporal spread of the STA (Fig. 6C) and I_{STA}^{Peak} (Fig. 6D), a significant increase in Q_{STA} (Fig. 6F), and a differential impact on T_{TCDW} (Fig. 6H) and T_{ECDW} (Fig. 6I) based on the value of $\bar{g}_h$. We also noted that the relationship between the impedance-based resonance frequency (f_R) and f_{STA} (both computed with the same model parameters) exhibited an inverse correlation with
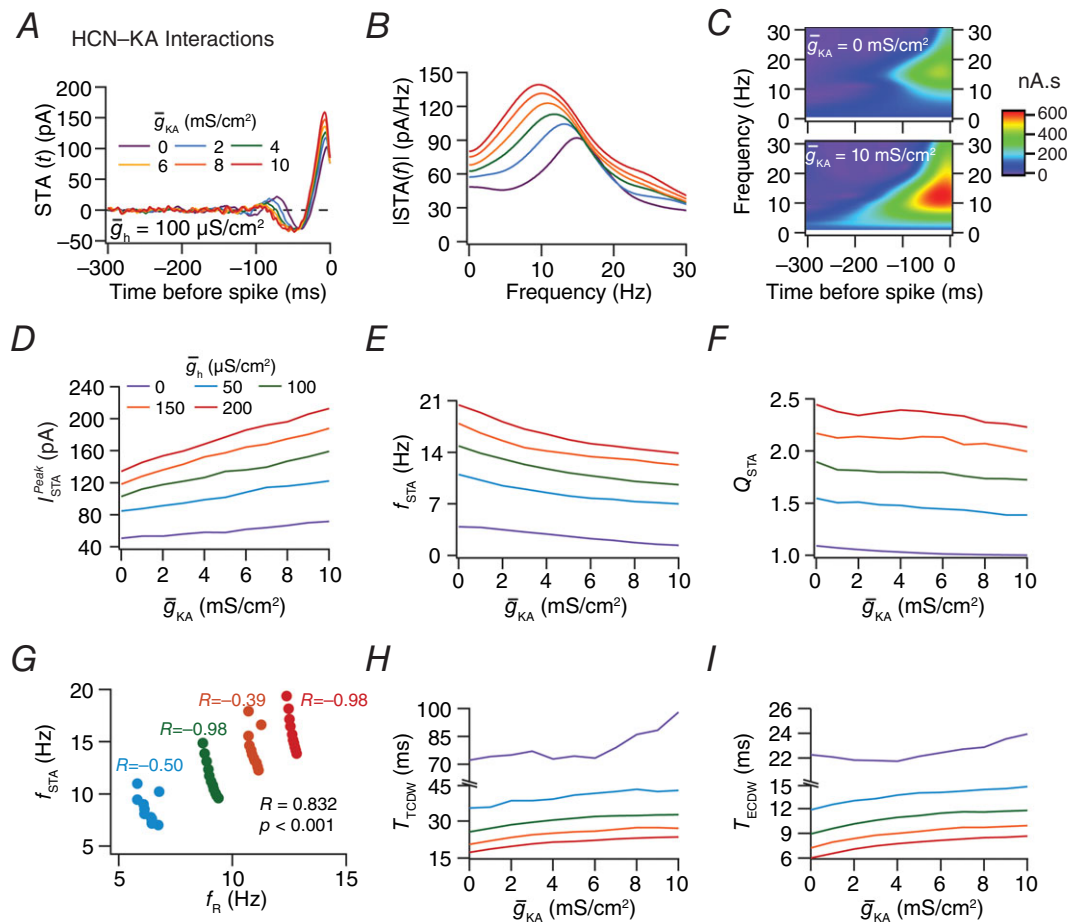

Figure 5. KA channels interacted with HCN channels to modulate STA spectral selectivity and the coincidence detection window

A, the class II/III STA consequent to the introduction of HCN channels in the model was regulated by the additional presence of KA channels. *B*, the Fourier transform of the STA revealed a band-pass structure with an increase in STA amplitude at both the STA characteristic frequency as well as at zero frequency. *C*, wavelet analysis of the STA revealed a spectrotemporal broadening of the frequency selectivity in the presence of higher KA channels. *D*, $\bar{g}_{CaT}$ increased with increasing density of KA, and this increase was higher for higher density of HCN channels. The labels specified in *D* hold for panels *D–I*. *E*, the decrease in f_{STA} with increase in density of KA channels was enhanced by the presence of a higher density of HCN channels. *F*, Q_{STA} decreased with increasing density of KA channels for all values of HCN conductance. *G*, correlation between impedance-based resonance frequency (f_R) and STA characteristic frequency (f_{STA}) plotted for various values of $\bar{g}_{KA}$ and $\bar{g}_h$. The individual *R* values correspond to Pearson's correlation coefficient for the f_R *vs.* f_{STA} plot computed for a set value of $\bar{g}_h$ across different values of $\bar{g}_{KA}$. The total *R* value corresponds to Pearson's correlation coefficient computed for the f_R *vs.* f_{STA} plot across all values of $\bar{g}_h$ and $\bar{g}_{KA}$. Note inverse correlations with reference to all individual *R* values. *H* and *I*, the total (*H*) and effective (*I*) CDWs increased with increasing density of KA channels. $\bar{g}_{Na} = 30$ mS cm^{-2}, $\bar{g}_{KDR} = 2$ mS cm^{-2} and $\sigma_{noise} = 1.8$ nA. Sensitivity analyses with reference to various parameters of KA channels are presented in Table 3, and its interactions with HCN channels are analysed in Table 4.

Table 4. Sensitivity analysis for STA and CDW measurements in a single compartmental model when potassium channels and HCN channels were co-expressed

Parameters	Tested range	I_{STA}^{Peak}	f_{STA}	Q_{STA}	T_{TCDW}	T_{ECDW}
$\overline{g}_{KA}$ (μS cm^{-2})	0–10	Increased	Decreased	Decreased*	Increased	Increased
$\overline{g}_{h}$ (μS cm^{-2})	0–200	Increased	Increased	Increased	Decreased	Decreased
$V_{1/2,act}$ KA (mV)	−10 to 30	Decreased	Increased	Increased	Decreased*	Decreased*
$V_{1/2,inact}$ KA (mV)	−120 to 0	Increased	Decreased	Increased	Increased*	Increased*
τ_{act} KA (ms)	0.02–0.65	Decreased	Increased*	Decreased*	Decreased*	Decreased*
τ_{inact} KA (ms)	2–90	Increased*	Decreased*	Increased*	Increased*	Increased*
$V_{1/2,act}$ HCN (mV)	−120 to 0	Sigmoidal increase	Bell-shaped	Bell-shaped	U-shaped	U-shaped
τ_{act} HCN (ms)	3.3–191.9	Decreased	Asymmetric bell-shaped	Asymmetric bell-shaped	U-shaped*	U-shaped*

These simulations were performed in the presence of KA, HCN, NaF and KDR channels. Changes in the STA-derived measures are with respect to increase in parameter values. Increases in the voltages (V_m and $V_{1/2}$) indicate shifts towards more depolarized potentials. Default $\overline{g}_{KA}$ = 5 mS cm^{-2}; $\overline{g}_{h}$ = 100 μS cm^{-2}. Also see Fig. 6. *Small (<10%) change.

changes exclusively in NaP channel density (Fig. 6*G*). This inverse correlation is a direct consequence of a differential impact of NaP channels on f_R and f_{STA}. Although the magnitudes of changes were relatively small, an increase in NaP conductance reduced f_R but increased f_{STA} (Fig. 6*E*).

In summary, results from our pair-wise interaction analyses (Figs 4–6) demonstrate that CaT channels synergistically interact with HCN channels to increase the strength and frequency of STA spectral selectivity, apart from reducing the coincidence detection window (Fig. 4). The presence of KA channels along with HCN channels had an impact similar to the presence of an additional leak conductance (Fig. 1*I–L*, $g_{leak} = 1/R_m$; Das & Narayanan, 2014), expected because of the large window component present in hippocampal KA current (Kim *et al.* 2005; Rathour & Narayanan, 2012*a*). Specifically, the additional presence of KA channels reduced the strength and frequency of STA spectral selectivity, apart from increasing the coincidence detection window (Fig. 5). Finally, the major contribution of the additional presence of NaP channels was a significant increase in the strength of STA spectral selectivity, with marginal changes in other parameters (Fig. 6). Importantly, our analyses also uncovered significant dissociations between f_R and f_{STA}, which assumed different values for identical models and exhibited inverse relationships with changes in certain channel conductances (Figs 4*G*, 5*G* and 6*G*).

Spike initiation dynamics exhibited strong coincidence-detector attributes in a morphologically precise model endowed with multiple realistic VGIC gradients

Thus far, we analysed the roles of kinetic pair-wise interactions in regulating spike initiation dynamics and coincidence detection in a single compartmental model. However, hippocampal pyramidal neurons are endowed with complex dendritic arborization comprising several ion channels with non-uniform expression profiles (Magee & Johnston, 1995; Hoffman *et al.* 1997; Magee, 1998; Johnston & Narayanan, 2008). To assess the role of kinetic as well as spatial (Rathour & Narayanan, 2012*b*) interactions among these channels in regulating STA and CDW, we employed a morphologically realistic model (Fig. 7*A*) with several physiologically realistic channel gradients (see Methods), adopted from (Rathour & Narayanan, 2014). These gradients and associated passive properties were set such that the functional maps of input resistance, backpropagating action potential amplitude, local resonance frequency and transfer resonance frequency along the somato-apical trunk (Fig. 7*B*) matched experimental observations (Hoffman *et al.* 1997; Magee, 1998; Narayanan & Johnston, 2007, 2012; Rathour & Narayanan, 2012*a*; Vaidya & Johnston, 2012).

We computed the STA at different locations along the somato-apical trunk of the model and quantified the associated measurements. Whereas the somatic STA was typically class I with the SPPL of the STA extending over a time period of ~50 ms (in the order of the membrane time constant), the dendritic STA became progressively more class II/III with increase in distance from the soma (Fig. 7*C*). The distal dendritic STA displayed a deep negative lobe, resulting in a very narrow window over which the inputs were positively weighted (Fig. 7*C*). Spectrotemporal analysis of the STA revealed strong spectral selectivity confined to the period just preceding the spike, especially in distal STA (Fig. 7*D*). Of the STA measurements, whereas I_{STA}^{Peak} reflected changes in R_{in} (Fig. 7*B*) with initial increases transforming to reductions at the distal-most locations (Fig. 7*E*), both f_{STA} and Q_{STA} increased with distance from the soma (Fig. 7*F*). These results suggested that the presence of multiple ion-channel gradients along the somatodendritic axis translated to an I–CD continuum of spike initiation dynamics, with

significant parts of the neuron exhibiting strong class II/III characteristics in their STA.

Somatodendritic locations in a morphologically realistic active dendritic tree displayed an effective coincidence detection window in the fast gamma/epsilon band

Next, we quantified the coincidence detection capabilities of the active somatodendritic structure endowed with these several ion channel gradients. Whereas the total

CDW decreased from ~50 ms at the soma to less than 20 ms at the distal-most location along the apical dendrite (Fig. 7G), the effective CDW was much lower (~6–10 ms), and corresponded to the fast gamma and epsilon frequency bands (Freeman, 2007; Colgin *et al.* 2009; Colgin & Moser, 2010; Bieri *et al.* 2014). We noted that the non-monotonic trend in the T_{ECDW} is a direct consequence of the dependence of T_{ECDW} on the STA amplitude in the SPPL (eqn (6)), which exhibited non-monotonic features (Fig. 7E). Together, whereas the STA kernels at various locations along the dendritic axis of the neuron exhibited theta-frequency selectivity (Fig. 7F), the effective
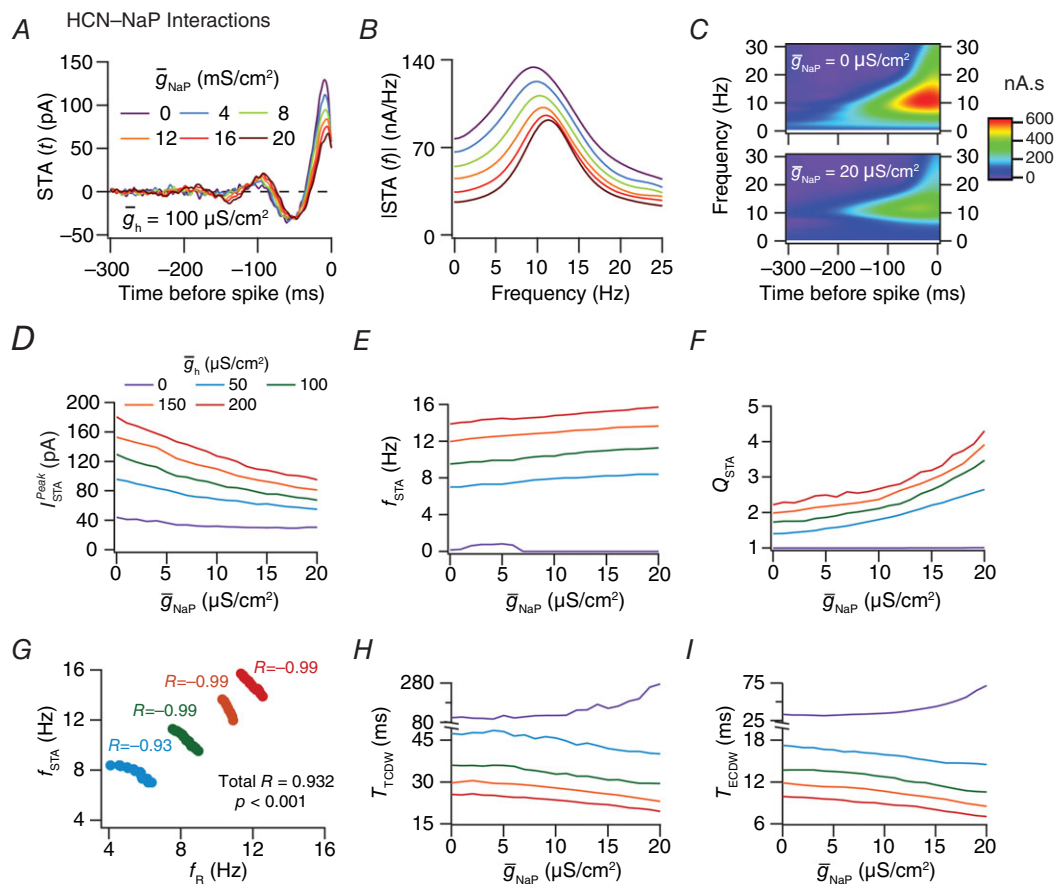

Figure 6. NaP channels strongly modulated the gain of the neuron and the strength of frequency selectivity in the presence of HCN channels
A and *B*, the class II/III STA (*A*) and its band-pass spectral structure (*B*) revealed the emergence of a sharply tuned spectral selectivity with increasing density of NaP channels. *C*, wavelet analyses evinced sharply tuned theta-frequency selectivity with higher density of NaP channels. *D*, I_{STA}^{Peak} decreased with increasing density of NaP channels, with the percentage of this reduction boosted with increase in HCN channel density. The labels specified in *D* hold for panels *D*–*I*. *E*, f_{STA} exhibited a small increase with increase in NaP channel density. *F*, Q_{STA} increased dramatically with increase in the density of NaP channels. *G*, correlation between impedance-based resonance frequency (f_R) and STA characteristic frequency (f_{STA}) plotted for various values of $\bar{g}_{NaP}$ and $\bar{g}_h$. The individual *R* values correspond to Pearson's correlation coefficient for the f_R *vs.* f_{STA} plot computed for a set value of $\bar{g}_h$ across different values of $\bar{g}_{NaP}$. The total *R* value corresponds to Pearson's correlation coefficient computed for the f_R *vs.* f_{STA} plot across all values of $\bar{g}_h$ and $\bar{g}_{NaP}$. Note inverse correlations with reference to all individual *R* values. *H* and *I*, the sensitivity of total (T_{TCDW}; *H*) and effective (T_{ECDW}; *I*) CDWs to increase in NaP channels was differential, depending on the density of HCN channels. $\bar{g}_{Na} = 18$ mS cm^{-2}, $\bar{g}_{KDR} = 0.7$ mS cm^{-2} and $\sigma_{noise} = 1.5$ nA. Sensitivity analyses with reference to various parameters of NaP channels are presented in Table 5, and its interactions with HCN channels are analysed in Table 6.

coincidence detection windows across somatodendritic locations were in the fast gamma/epsilon frequency band (Buzsaki, 2006; Freeman, 2007; Colgin *et al.* 2009; Colgin & Moser, 2010) as a consequence of active dendrites.

Spike initiation dynamics exhibited adaptation to the input statistics

The linear kernel of the neuron is known to be sensitive to the statistics of the stimulus used to compute it and undergoes a temporal compaction with increase in the stimulus variance (Enroth-Cugell & Shapley, 1973; Agüera y Arcas *et al.* 2003; Yu & Lee, 2003; Nagel & Doupe, 2006; Hong *et al.* 2007; Mato & Samengo, 2008; Famulare & Fairhall, 2010; Das & Narayanan, 2014). In agreement with these studies, we found that an increase in σ_{noise} resulted in an increase in I_{STA}^{Peak}, f_{STA} and Q_{STA}, accompanied by a reduction in the total and effective CDW (Fig. 7*H–K*). However, the changes in f_{STA}, Q_{STA} and the CDW measurements introduced by altering σ_{noise} were marginal in the distal location because the sodium channels in distal dendrites recover slowly from inactivation (Colbert *et al.* 1997; Das & Narayanan, 2014).
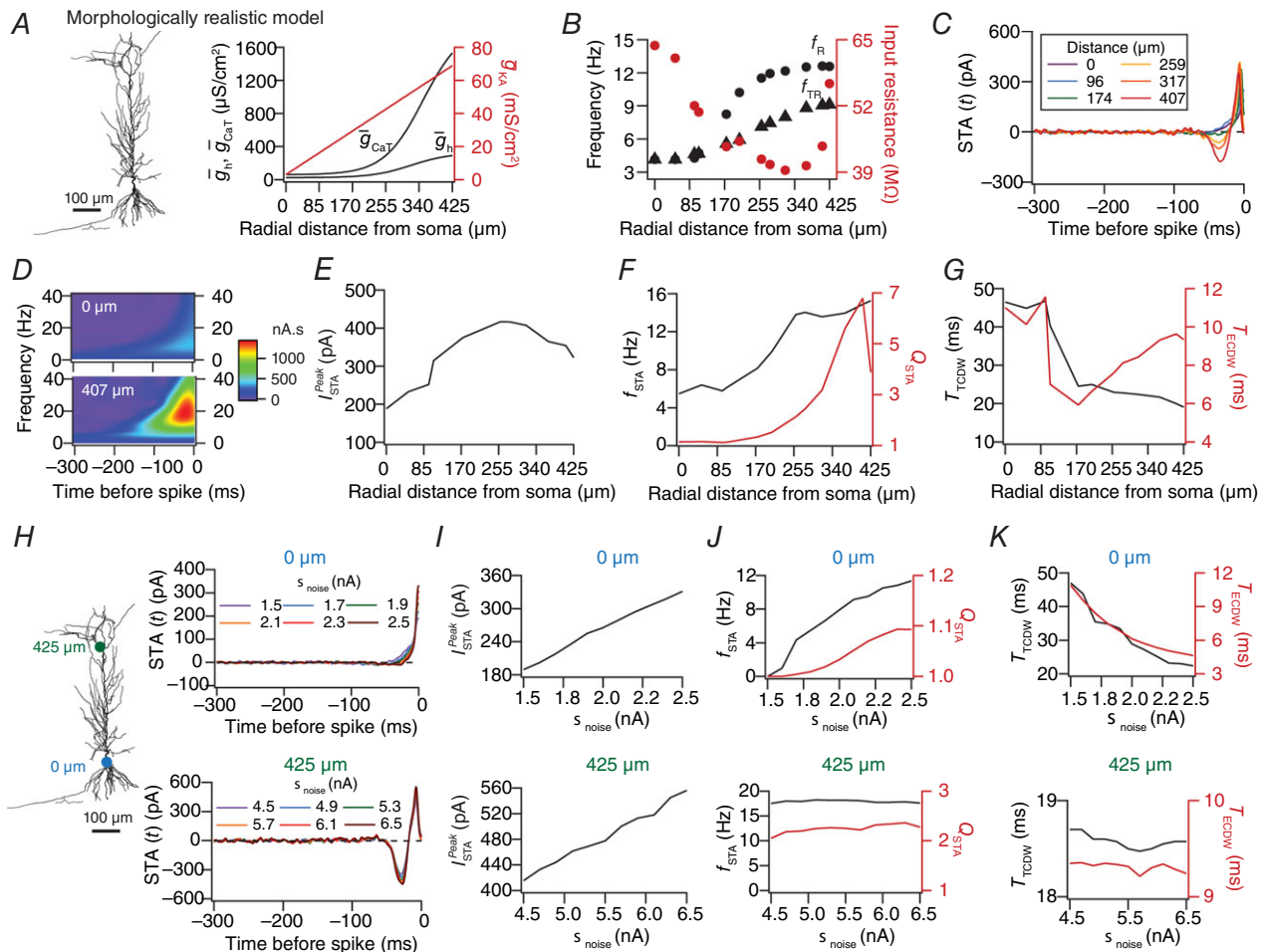

Figure 7. Stratified gamma-frequency range coincidence detection and adaptation to stimulus statistics in a morphologically realistic model with physiologically constrained ion channel gradients
A and *B*, a morphologically realistic model (*A*; left) with gradients in densities of HCN, CaT and KA channels (*A*; right), where various physiological measurements matched their experimental counterparts (*B*). *C*, the STA revealed a clear transition from class I for proximal dendritic locations to class II/III for distal dendritic locations. *D*, wavelet analysis revealed a strong theta-frequency selectivity temporally localized to ~100 ms before the spike for the distal dendritic location. *E*, I_{STA}^{Peak} increased with distance from the soma, but decreased for the distal-most locations. *F*, f_{STA} and Q_{STA} increased as functions of distance from the soma. *G*, the CDW decreased with distance from the soma, and the effective CDW showed a non-monotonic variation due to the non-monotonic variation in STA amplitude by which it is weighted. For *C–G*, σ_{noise} varied with location. *H–K*, simulations were performed to assess the dependence of the STA (*H*) on σ_{noise}. I_{STA}^{Peak} (*I*), f_{STA}, Q_{STA} (*J*) and the total and effective CDW (*K*) plotted as functions of σ_{noise}, with measurements from the soma (top) and a dendritic location 425 μm away from the soma (bottom). $\bar{g}_{Na} = 16$ mS cm^{-2}, $\bar{g}_{KDR} = 10$ mS cm^{-2}.

These results are consistent with earlier observations that the adaptation of neuronal STA to stimulus variance is largely mediated by spike-generating currents in the neuron, which serve as a feedback mechanism responding to increased firing frequency (Famulare & Fairhall, 2010; Urdapilleta & Samengo, 2015).

Removal of active dendritic channels abolished spectral selectivity in spike initiation dynamics and exhibited large integration time windows

What roles did dendritic ion channels play in conferring location-dependent theta-frequency spectral selectivity and gamma-frequency CDW on the neuronal somatodendritic axis (Fig. 7)? To address this, we removed all somatodendritic VGICs except for the spike-generating NaF and KDR channels inserted only in the soma and the axon initial segment, which resulted in large values of R_{in} that increased with distance from the soma (Mishra & Narayanan, 2015). Upon analysing these passive dendritic structures, we found that the STA underwent a distinct transition to class I for all somatodendritic locations, with the SPPL of the STA extending over a time period of ~400 ms, indicating that inputs are being integrated over longer temporal durations compared to

active dendritic structures (Fig. 8B; cf. Fig. 7C where the SPPL is ~20–50 ms). The Fourier transform of the STA at different somatodendritic locations revealed a typical low-pass structure (Fig. 8C), which was further confirmed by the absence of any frequency selectivity as evinced from the wavelet analysis (Fig. 8D). Concordantly, f_{STA} was zero and Q_{STA} was ~1 across all locations. I_{STA}^{Peak} decreased with distance from the soma (Fig. 8E), reflecting the distance-dependent increase in R_{in} of a passive tree (Fig. 8A), the total CDW was around 400 ms across the entire dendritic tree and the effective CDW increased with distance from the soma (Fig. 8F). Together, the removal of the dendritic ion channels abolished frequency selectivity in spike initiation dynamics and transformed the neuron to a class I integrator.

Morphologically precise model endowed with uniformly distributed HCN and CaT channels exhibited class I STA with narrow integration window

Given the dependence of f_{STA} on resonating conductances and their interactions (Figs 1, 3 and 4), we asked if the gradient in f_{STA} was indeed dependent on the gradient in resonating conductances (HCN and CaT). To answer this, we utilized the model analysed in Fig. 7, but
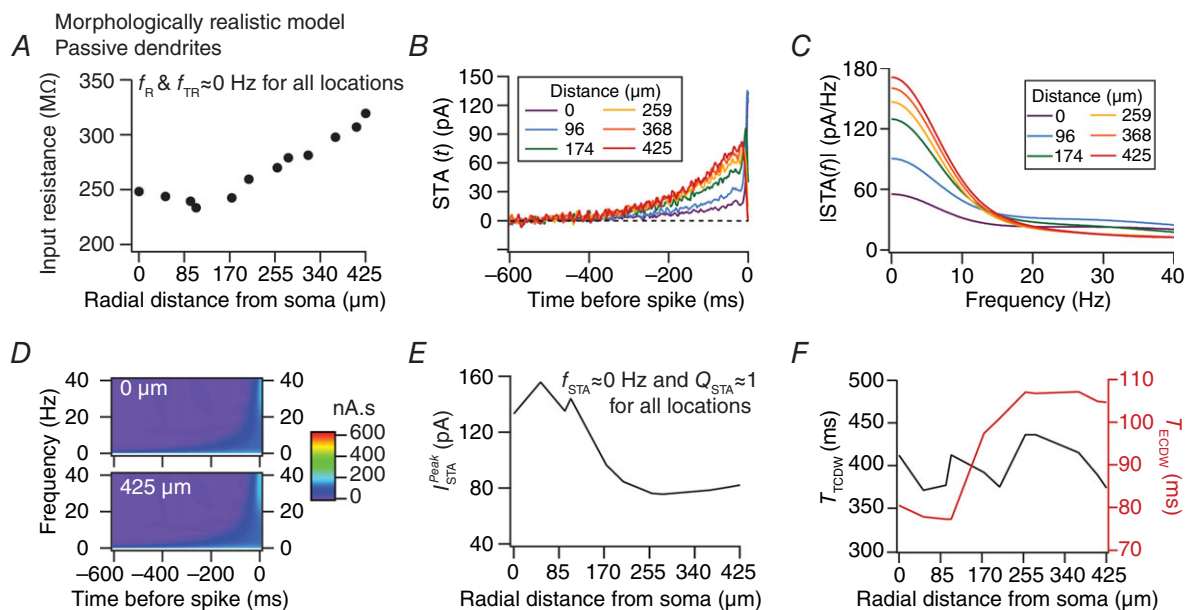

Figure 8. A morphologically realistic model with a passive dendritic tree exhibited class I STA with a large integration time window
For all simulations here, the dendritic tree was completely passive, and spike-generating conductances were included exclusively in the soma and the axonal initial segment. *A*, input resistance increased with distance, and there were no local or transfer resonances across all locations. *B*, the STA was typically class I with the positive lobe extending to ~400 ms for all locations. *C*, Fourier transform of the STA from *B* revealed a typical low-pass structure. *D*, wavelet analysis revealed absence of frequency selectivity for both somatic and distal dendritic locations. *E*, I_{STA}^{Peak} decreased with distance from the soma. f_{STA} was ~0 Hz and Q_{STA} was 1, indicating the absence of STA spectral selectivity for all locations. *F*, the total CDW increased with distance from the soma, while the effective CDW was mostly constant throughout. $\bar{g}_{Na} = 41$ mS cm^{-2}, $\bar{g}_{KDR} = 53$ mS cm^{-2} and σ_{noise} varied with location.

altered only the HCN and CaT channel distributions such that they were expressed at uniform density throughout the somatodendritic arbor (Fig. 9*A*). For each of these two channels, this density was computed by uniformly redistributing the total conductance obtained with the respective distribution specified in Fig. 7*A*, so that the total conductance values across the neuron was the same as Fig. 7. Although R_{in} decreased with distance from the soma with slightly higher values, both local and transfer resonance frequencies were significantly lower when compared to the tree with gradients in both the resonating conductances (Fig. 9*B*; cf. Fig. 7*B*). These are to be expected given the measurement-dependent contributions of spatial interactions among ion channels expressed across the somatodendritic arbor (Rathour & Narayanan, 2012*b*).

The STA underwent a distinct transition to class I for all dendritic locations; however, the SPPL of the STA was narrow compared to the passive dendritic tree (Fig. 9*C*; cf. Fig. 8*B*). The Fourier and wavelet transforms of the STA for several locations revealed a low-pass structure, with distal locations manifesting weak ($Q_{STA} \approx 1$ across all locations) spectral selectivity (Fig. 9*D–F*). I_{STA}^{Peak} increased monotonically with distance from the soma (Fig. 9*F*), reflective of the reduced R_{in} at distal locations (Fig. 9*B*). Although the STA did not manifest the negative

lobes characteristic of class II/III, the total and effective integration/coincidence detection time windows obtained here were comparable to those in dendritic trees endowed with resonating conductance gradients (Fig. 9*G*; cf. Fig. 7*G*).

Together, our results with passive dendritic structures (Fig. 8) and dendritic structures with uniform resonating conductance gradients (Fig. 9) demonstrate the critical importance of gradients in resonating conductances in defining class II/III STA endowed with strong location-dependent theta-frequency selectivity and gamma-band coincidence detection windows (Fig. 7) across somatodendritic compartments.

CDW assessed with pairs of synaptic inputs corroborated the role of VGIC gradients in mediating location-dependent gamma-range coincidence detection

Finally, to validate our conclusions on coincidence detection windows based on measurements from the STA, we employed a more conventional measure of coincidence detection of paired excitatory synaptic potentials arriving at various somatodendritic locations with different input frequencies (interpulse interval, IPI). For each of the
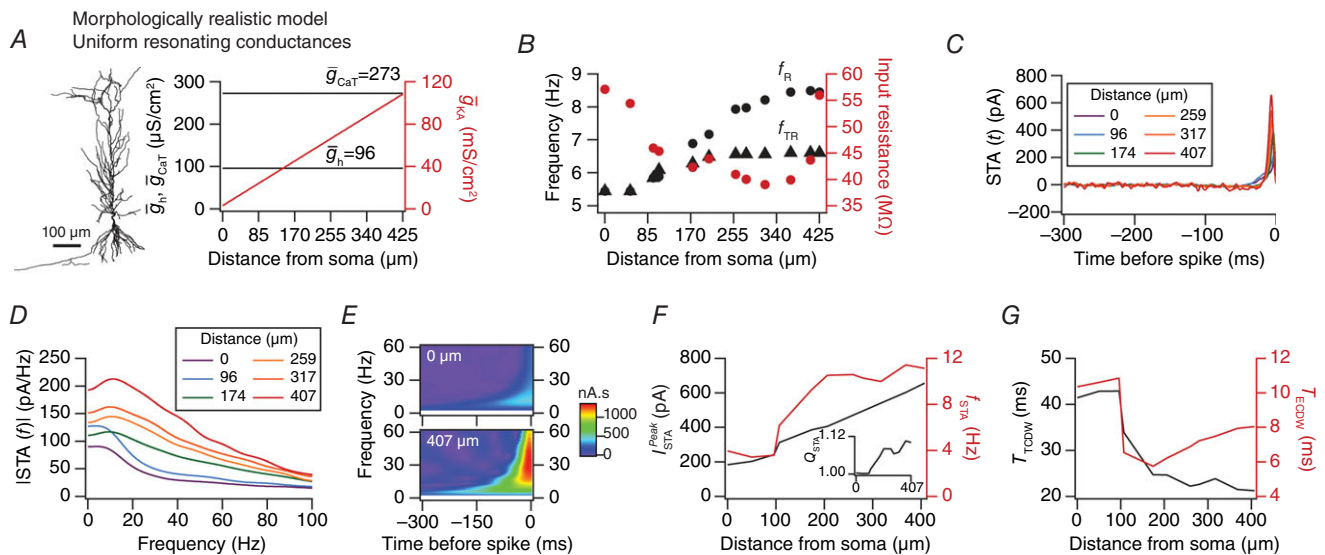

Figure 9. The STA was class I and theta-frequency selectivity absent in a morphologically realistic model with uniform somatodendritic distribution of HCN and CaT channels
A, a morphologically realistic model with constant densities (corresponding to uniform redistribution of total conductance values from the distribution represented in Fig. 7*A*) of HCN and CaT channels and a gradient in KA channels was used. *B*, input resistance (R_{in}), local (f_R) and transfer resonance frequency (f_{TR}) as functions of distance from the soma. *C*, the STA was typically class I with the positive lobe becoming narrower for distal dendritic inputs. *D*, Fourier transform of the STA from *C* revealed a low-pass structure. *E*, wavelet analysis revealed the absence of frequency selectivity for the somatic location and a high-frequency selectivity for the distal-most dendritic location. *F*, I_{STA}^{Peak} increased with distance from the soma. f_{STA} increased for distal locations but was accompanied by a $Q_{STA} = \sim 1$ (inset) indicating weak spectral selectivity. *G*, the total CDW decreased with distance from the soma and the effective CDW showed a non-monotonic decrease with distance. $\bar{g}_{Na} = 16$ mS cm^{-2}, $\bar{g}_{KDR} = 10$ mS cm^{-2} and σ_{noise} varied with location.

different channel configurations (analysed in Figs 7–9), we found the largest IPI (or smallest frequency), IPI_{Max}, that would elicit a somatic action potential in response to the second (but not the first) of the paired synaptic potentials. IPI_{Max} was then treated as a direct measure of the coincidence detection window, as it constitutes the maximum interval between two depolarizing inputs for which coincidence can be detected through a somatic spike. For each location IPI_{Max} was computed with various synaptic strengths, and the average computed from these different IPI_{Max} values was considered a measure of the coincidence detection window.

For the morphologically realistic model with passive dendrites (Fig. 8), we found the average IPI_{Max} to be $\sim$300 ms across the dendritic tree (Fig. 10*A* and *B*; cf. Fig. 8*F*), suggesting passive integration of the EPSPs over large integration time windows. When uniform densities of CaT and HCN channels were introduced in the presence of a KA gradient (Fig. 9) in the somatodendritic compartments, the average IPI_{Max} was narrow, ranging from $\sim$30 ms at the soma to $\sim$10 ms at the distal dendrites (Fig. 10*C*; cf. Fig. 9*G*). Finally, in the model with all ion channel gradients intact (Fig. 7), we found the coincidence detection window to be in the gamma frequency range, with distal compartments requiring inputs to arrive at lower values of IPI (higher frequencies) for coincidence to occur (Fig. 10*D* and *E*). Somatic voltage traces here also revealed a key difference in the somatic response observed from that in the passive model. When successful coincidence detection occurred (at the IPI_{Max}), a single somatic action potential was generated after the second EPSP (Fig. 10*D*) instead of a train of action potentials when integration of the EPSPs was occurring in the passive model (Fig. 10*A*), owing to differences in excitability (see Figs 7 and 8). Together, these results employing coincidence detection of paired EPSPs along the somatodendritic trunk corroborated our conclusions on the ability of hippocampal dendrites endowed with ion channel gradients to perform location-dependent gamma-range coincidence detection.

In summary, these results uncover critical relationships between the channels expressed by a neuronal compartment and its physiological properties, including spectral selectivity in the STA and the ability to perform coincidence detection at a given frequency range. Our analyses provide direct evidence that a narrowing of the SPPL of the neuronal kernel translates to the ability of the neuronal compartment to detect temporal proximity of inputs at higher frequencies. Specifically, the presence of high densities of resonating conductances (HCN and CaT) in hippocampal and cortical neurons (Magee & Johnston, 1995; Magee, 1998; Williams & Stuart, 2000; Kole *et al.* 2006), in conjunction with the several dendritic spike-generating conductances (NaF, CaT and NMDA receptor) in their dendrites (Schiller *et al.* 1997, 2000;

Stuart *et al.* 1997; Polsky *et al.* 2004; Larkum *et al.* 2009) ensure that these neurons and their dendrites are endowed with abilities to detect high-frequency input coincidence. These results also suggest that the presence of gradients in resonating conductances and their interactions with other conductances mediates several functional maps, including those in f_{STA}, Q_{STA} and the window of coincidence detection (Fig. 10*F*). The distance-dependent reduction in the CDW that is consequent to the presence of gradients in resonating conductances also provides a putative mechanism for a neuron to perform coincidence detection of slow *versus* fast gamma inputs arriving at proximal *versus* distal locations (Colgin *et al.* 2009; Colgin & Moser, 2010; Bieri *et al.* 2014), respectively (Fig. 10*F*). Together, these results provide an overarching hypothesis for the role of dendritic gradients in VGICs in pyramidal neurons in mediating location-dependent feature selectivity and coincidence detection of inputs, allowing for differential processing of information along the dendritic arbor (Fig. 10*F*).

Discussion

The principal conclusion of this study is that spatiotemporal interactions among resonating conductances and other VGICs lead to the robust emergence of gamma-frequency coincidence detection windows and of strong theta-frequency selectivity in the STA of hippocampal model neurons. The several quantitative metrics that we derived for CDW unveil the specific frequency ranges for coincidence detection windows in the presence and absence of resonating conductances, besides assigning specific roles for the several coexpressing subthreshold ion channels. Our analyses revealed the differential contributions of six different conductances in placing location-dependent spike initiation dynamics at different points along the I–CD continuum, with co-operation and competition among these channels determining the specific attributes of the STA in a state-dependent manner. Additionally, the spatiotemporal interactions between these VGICs assign specific frequency ranges for location-dependent CDW, thereby determining the ability of a neuron to parse afferent inputs into specific temporal packets.

Gradients in active conductances bestow location-dependent gamma-frequency coincidence detection windows on neuronal dendrites

Neurons exhibit clear gamma frequency spike phase preferences and have been postulated to construct cell-assembly readers that treat spikes that fall within a gamma cycle as a single event (Buzsaki, 2006; Senior *et al.* 2008; Buzsaki, 2010; Colgin & Moser, 2010; Wang,

2010; Buzsaki & Wang, 2012; Lisman & Jensen, 2013). The organization of such cell assemblies within individual cycles of the gamma oscillations engender the need for downstream neurons that can detect activity synchronized at gamma frequencies, with the integration window not spilling over to the next gamma cycle. Further, within a CA1 pyramidal neuron, whereas the entorhinal cortex

routes information to the distal dendritic regions in the fast gamma band, the proximal inputs from the CA3 are routed in the slow gamma band, thereby coordinating different spatial coding modes in these neurons (Colgin *et al.* 2009; Colgin & Moser, 2010; Bieri *et al.* 2014). These effectively translate to a decoding requirement on CA1 pyramidal neurons that the CDW at distal dendritic
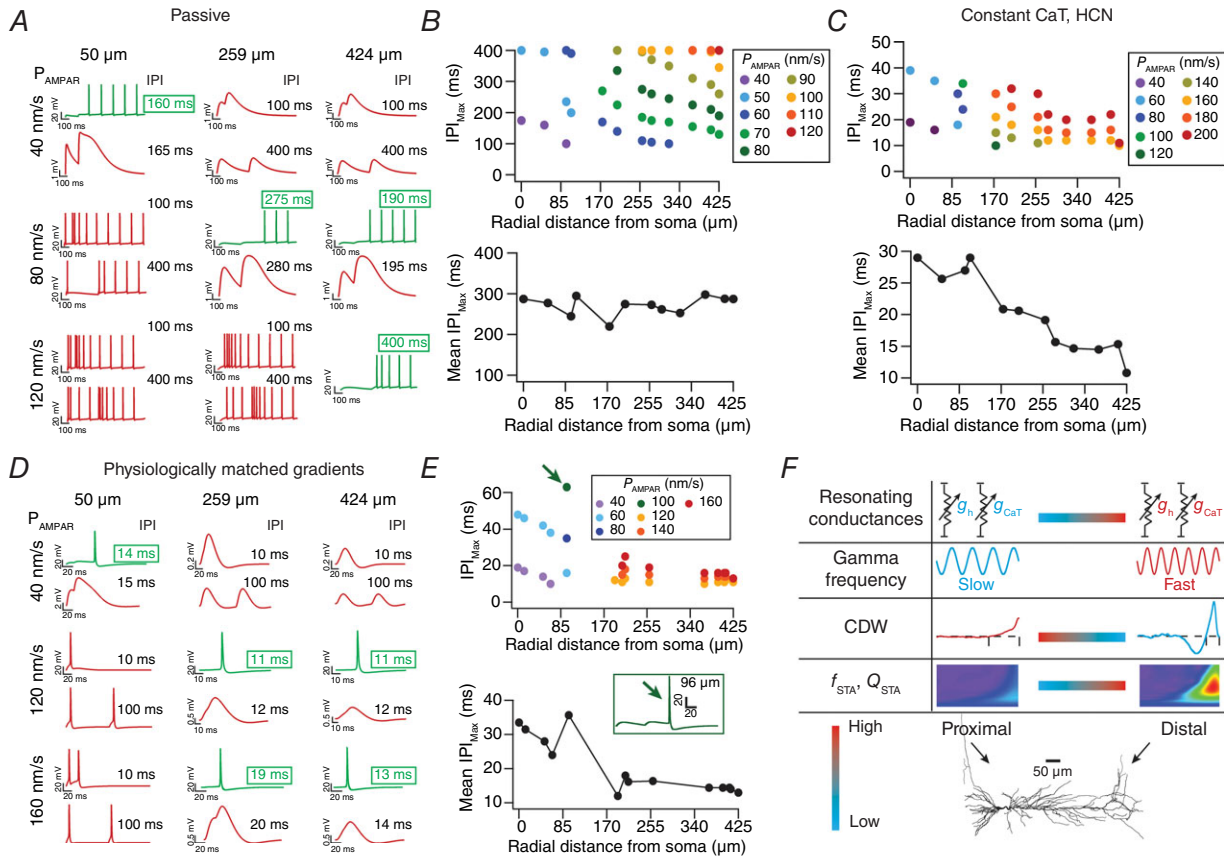

Figure 10. Coincidence detection with pairs of EPSPs revealed stratified gamma range coincidence detection in a morphologically realistic model with physiologically constrained ion channel gradients
A, in a passive morphologically realistic model (Fig. 8), somatic voltage traces in response to injection of pairs of EPSPs with different values of interpulse intervals (IPIs). Traces at different dendritic locations with different values of AMPAR permeability, $\overline{P}_{AMPAR}$, are shown. Traces corresponding to boxed IPI values represent valid cases where the action potentials were generated in response to integration of both the EPSPs. The traces with IPI values without borders represent cases where either the first EPSP alone was sufficiently strong to generate action potentials or the strength of the EPSPs were not sufficient for the paired EPSPs to generate action potentials. The value of IPI_{Max} is highlighted in bold for all cases of valid response. *B*, IPI_{Max}, measured with different permeability values, plotted as a function of distance at which the stimulus was presented (top). The average IPI_{Max}, averaged over all permeability values tested for a given location, was ~300 ms across locations (bottom). *C*, same as *B*, for the case where the densities of CaT and HCN channels were uniform across the somatodendritic trunk (Fig. 9). A decrease in the IPI_{Max} was observed with distance for all permeability values. *D*, same as *A*, for the morphologically realistic model with physiologically constrained gradients in CaT, HCN and KA (Fig. 7). Note that coincidence detection of the EPSPs resulted in generation of a single somatic action potential after the second EPSP, contrary to the passive case where multiple action potentials were observed (*A*). *E*, same as *B*, for the model used in *D* (Fig. 7). Inset shows the voltage trace for the case where the IPI_{Max} was relatively large (56 ms) for permeability value of 100 nm s^{-1} (arrow in top panel). It may be noted that the increase in IPI_{Max} was consequent to the late arrival of the coincident spike, probably owing to the inactivation of transient K$^+$ channels. *F*, a schematic diagram depicting the increase in resonating conductance density, the resultant increase in the f_{STA} and Q_{STA}, the transition from slow to fast gamma inputs and decrease in CDW along the somatodendritic axis of CA1 pyramidal neurons. The bar on the bottom left provides the code for the High–Low transition that is employed with reference to each physiological measurement depicted.

locations receiving fast gamma inputs has to be narrower than that at proximal locations receiving slow gamma inputs.

Against this, we noted that the two resonating conductances (HCN and CaT) that endow neurons with a narrow CDW express at progressively higher densities along the somatodendritic axis of CA1 pyramidal neurons. As a consequence of the inverse relationship between the density of these channels and the CDW (Figs 1 and 2), the synergistic interaction between these two channels in reducing the CDW (Fig. 3), and the propensity for the generation of dendritic spikes at distal locations (Figs 7 and 9), our results reveal a reduction in the CDW with increase in distance from the soma (Figs 7 and 10). Importantly, despite the slow integration mode that should be expected (e.g. Fig. 8), from a passive membrane time constant of ~40 ms (Golding *et al.* 2005; Narayanan & Johnston, 2008*b*), the effective CDW is in the gamma range of frequencies suggesting that the presence of these resonating conductances enables neurons to detect gamma frequency coincidence of afferent inputs (Figs 7–10). Together, we postulate that gradients in dendritic resonating conductances enable graded gamma frequency coincidence detection in hippocampal pyramidal neurons, with proximal and distal dendritic regions tuned for slow and fast gamma oscillatory inputs, respectively (Figs 7*G* and 10*E*). Finally, the high density of HCN channels in cortical pyramidal dendrites (Williams & Stuart, 2000; Kole *et al.* 2006) could endow cortical neurons with the ability to perform coincidence detection at gamma frequencies, thereby aiding cross-modal interactions that influence perception and decision-making processes (Llinás *et al.* 1998; Tallon-Baudry & Bertrand, 1999; Engel & Singer, 2001; Llinás *et al.* 2002; Wang, 2010).

Dissociations and relationships between resonance in impedance amplitude and spectral selectivity in spike initiation dynamics

A well-studied form of spectral selectivity in neuronal compartments is that with reference to resonance in the impedance amplitude profile (Cole & Baker, 1941; Cole, 1968; Hutcheon & Yarom, 2000). In hippocampal pyramidal neurons, at least two forms of resonance are known to exist, one mediated by HCN channels and the other by M-type K^+ channels (Pike *et al.* 2000; Hu *et al.* 2002). The first experimental and computational demonstration that a neuron is endowed with not one, but with several resonance frequencies depending on the location along the somatodendritic axis came from Narayanan & Johnston (2007, 2008*b*), and was further corroborated by evidence from Hu *et al.* (2009), Marcelin *et al.* (2009), Kalmbach *et al.* (2013), Zhuchkova *et al.* (2013) and Laudanski *et al.* (2014). The ionic basis

(Narayanan & Johnston, 2007, 2008*b*; Hu *et al.* 2009; Zemankovics *et al.* 2010; Rathour & Narayanan, 2012*a*; Kalmbach *et al.* 2013), emergence (Rathour & Narayanan, 2012*b*; Zhuchkova *et al.* 2013; Dhupia *et al.* 2015) and homeostasis (Rathour & Narayanan, 2012*a*, 2014) of this functional map in local resonance frequency (Narayanan & Johnston, 2012) are well explored through computational and experimental approaches. Whereas these analyses were with reference to local resonance, the dependence of transfer impedance resonance on dendritic location has also been explored (Ulrich, 2002; Hu *et al.* 2009; Vaidya & Johnston, 2012; Das & Narayanan, 2014; Laudanski *et al.* 2014; Dhupia *et al.* 2015).

Against this literature on impedance-based resonance, an important question is whether spectral selectivity in spike initiation dynamics (f_{STA}) is the same as resonance in impedance amplitude profiles (f_R). Our results from this study and the previous one (Das & Narayanan, 2014) clearly demonstrate the dissociation between f_R and f_{STA} along several lines. First, whereas f_R is a measure of overall subthreshold frequency selectivity, f_{STA} is a measure of the spectral features that *spike generation* is selective to (specifically during the few 100 ms period that precedes the spikes). Secondly and importantly, several studies have clearly demonstrated that spectral selectivity in spike initiation dynamics are observed even in the absence of resonating conductances that are essential to sustain impedance-based resonance (Agüera y Arcas & Fairhall, 2003; Agüera y Arcas *et al.* 2003; Prescott *et al.* 2006, 2008*a,b*; Hong *et al.* 2007; Prescott & Sejnowski, 2008; Higgs & Spain, 2009; Famulare & Fairhall, 2010; Kispersky *et al.* 2012; Mease *et al.* 2013; Ratté *et al.* 2013; Das & Narayanan, 2014; Fontaine *et al.* 2014), establishing that impedance-based resonance is *not required* to sustain STA spectral selectivity (also see Figs 1–4, for cases where the resonating conductance values were set to zero). Finally, there were significant differences in how f_R and f_{STA} reacted to interactions between ion channels (see inverse correlations between f_R and f_{STA} in Figs 4*G*, 5*G* and 6*G*). For instance, an increase in the KA conductance in the presence of HCN channels increased f_R (Rathour & Narayanan, 2012*a*) but reduced f_{STA} (Fig. 5*G*), similar to the impact of an increase in the leak conductance in increasing f_R (Narayanan & Johnston, 2008*b*) but reducing f_{STA} (Das & Narayanan, 2014).

Despite these dissociations, our studies uncover significant relationships between f_R and f_{STA} as well. First, there were significant correlations between f_R/f_{TR} and f_{STA} when impedance resonance was expressed (Das & Narayanan, 2014). Second, the independent presence of CaT channels is known to sustain resonance as a consequence of its slow inactivation kinetics (Hutcheon *et al.* 1994; Rathour & Narayanan, 2012*a*), a property that enables their independent presence to transform the STA to class II/III thereby sustaining spectral selectivity

Table 5. Sensitivity analysis for STA and CDW measurements in a single compartmental model corresponding to parameters associated with persistent sodium channels

Parameters	Tested range	I_{STA}^{Peak}	f_{STA}	Q_{STA}	T_{TCDW}	T_{ECDW}
C_m (μF cm^{-2})	0.5–1.2	Decreased	Decreased	Decreased*	Increased	Increased
R_m (Ω cm^2)	20–40	Decreased	Decreased*	Increased*#	Increased	Increased
V_m (mV)	−67 to −61	U-shaped	No change	U-shaped#	U-shaped*	U-shaped
$\bar{g}_{NaP}$ (μS cm^{-2})	0–20	Decreased	No change	Increased#	Increased	Increased
$V_{1/2,act}$ (mV)	−60 to −40	Increased	No change	Decreased#	Decreased	Decreased
τ_{act} KA (ms)	0.5–20	No change	No change	Increased#	Increased	Increased
$\bar{g}_{Na}$ (μS cm^{-2})	18–26	Decreased*	No change	Increased#	Decreased*	Decreased*
$\bar{g}_{KDR}$ (μS cm^{-2})	1–15	Increased	No change	Decreased#	Decreased	Decreased

These simulations were performed in the presence of NaP, NaF and KDR channels. Changes in the STA-derived measures are with respect to increase in parameter values. Increases in the voltages (V_m and $V_{1/2}$) indicate shifts towards more depolarized potentials. Default $\bar{g}_{NaP} = 10\ \mu$S cm^{-2}. See Fig. 8 for the cases where $\bar{g}_h = 0$ mS cm^{-2}. *Small (<10%) change. #Values are ~1.

Table 6. Sensitivity analysis for STA and CDW measurements in a single compartmental model when persistent sodium channels and HCN channels were co-expressed

Parameters	Tested range	I_{STA}^{Peak}	f_{STA}	Q_{STA}	T_{TCDW}	T_{ECDW}
$\bar{g}_{NaP}$ (μS cm^{-2})	0–20	Decreased	Increased	Increased	Decreased	Decreased
$\bar{g}_h$ (μS cm^{-2})	0–200	Increased	Increased	Increased	Decreased	Decreased
$V_{1/2}$ act NaP (mV)	−60 to −40	Increased	Decreased	Decreased	Increased	Increased
τ_{act} NaP (ms)	0.5–20	Increased	Decreased	Decreased*	Increased	Increased
$V_{1/2,act}$ HCN (mV)	−120 to 0	Sigmoidal increase	Bell-shaped	Bell-shaped	U-shaped	U-shaped
τ_{act} HCN (ms)	3.3–191.9	Decreased	Asymmetric bell-shaped	Asymmetric bell-shaped	U-shaped*	U-shaped*

These simulations were performed in the presence of NaP, HCN, NaF and KDR channels. Changes in the STA-derived measures are with respect to increase in parameter values. Increases in the voltages (V_m and $V_{1/2}$) indicate shifts towards more depolarized potentials. Default $\bar{g}_{NaP} = 10\ \mu$S cm^{-2}; $\bar{g}_h = 100\ \mu$S cm^{-2}. Also see Fig. 8. *Small (<10%) change.

in the spike initiation dynamics (Fig. 4). Third, consistent with the ability of CaT channels to augment the range of parameters over which HCN channels sustained sub-threshold resonance (Rathour & Narayanan, 2012*a*), the additional presence of CaT channels enhanced the impact of HCN channels on f_{STA} and Q_{STA} (Fig. 4). Finally, akin to their ability to enhance subthreshold resonance strength without much impact on f_R (Hutcheon *et al.* 1996; Hutcheon & Yarom, 2000), we found that the presence of NaP channels with HCN channels enhanced Q_{STA}, with a relatively lesser impact on f_{STA} (Fig. 8). These observations provide a more general role for subthreshold response properties in sculpting the features for which neuronal spikes exhibit their preferences (Ratté *et al.* 2013; Das & Narayanan, 2014).

Localization, modulation and plasticity of ion channels towards regulation of location dependence in STA spectral selectivity and coincidence detection

The VGICs that our study has shown to modulate STA spectral selectivity and coincidence detection are known to undergo behaviourally relevant neuromodulatory and activity-dependent regulation in the hippocampus and other brain regions (Pape, 1996; Hoffman & Johnston, 1999; Cantrell & Catterall, 2001; Perez-Reyes, 2003; Cerda & Trimmer, 2010; Shah *et al.* 2010; He *et al.* 2014; Shah, 2014). While this would imply the possibility of dynamic reconfiguration in the location-dependent kernels of neuronal dendrites (Das & Narayanan, 2014) and their CDW, future studies should focus on whether the rich repertoire of channels and their modulatory mechanisms present in hippocampal dendrites hampers or promotes functional stability of STA and CDW. Specifically, the subcellular localization and targeting of VGICs and their subunits, in the presence of neuro-modulatory and plasticity influence, is an extremely complex puzzle in neurons with extensive dendritic arborization (Lai & Jan, 2006; Narayanan & Johnston, 2008*a*; Vacher *et al.* 2008; Nusser, 2009; Hanus & Schuman, 2013; Rathour & Narayanan, 2014). Against this, our results suggest that the spectrotemporal properties of spike initiation dynamics and the exact nature of the integration/coincidence detection window are determined

by complex spatiotemporal interactions between several VGICs.

Our results also confirm previous observations that after-hyperpolarization (AHP) conductances (Prescott *et al.* 2006; Prescott & Sejnowski, 2008; Higgs & Spain, 2009; Famulare & Fairhall, 2010; Kispersky *et al.* 2012; Mease *et al.* 2013; Das & Narayanan, 2014) and stimulus statistics (Destexhe *et al.* 2003; Prescott *et al.* 2008*b*; Famulare & Fairhall, 2010; Ratté *et al.* 2013; Das & Narayanan, 2014) are critical modulators of the STA that can contribute to a switch in excitability across classes without altering subthreshold resonance properties. Specifically, with ion channel kinetics derived from hippocampal pyramidal neurons, although spike-generating conductances in an otherwise passive model were able to sustain spectral selectivity in the STA in a manner that was correlated with the fast AHP (Das & Narayanan, 2014), this spectral selectivity was weak and was in the delta-frequency range (Figs 1–4, cases where the resonating conductance was set to zero). Additionally, f_{STA} increased (Das & Narayanan, 2014) and the CDW measurements decreased with increase in stimulus variance (Fig. 7), a proxy for the increasing fluctuations under high-conductance states.

Given that the regulatory influence of several VGICs and stimulus statistics on STA and CDW measurements are overlapping (Tables 1–6; Figs 1–10), we postulate that several non-unique combinations of channels and their properties along with stimulus variations would lead to similar STA kernels and CDWs across the dendritic arbor. This implies that the maintenance of STA/CDW homeostasis across the dendritic arbor is not contingent upon individual channelostasis, and collective forms of channelostasis are sufficient for functional homeostasis (Marder & Goaillard, 2006; Rathour & Narayanan, 2012*a*; O'Leary *et al.* 2014; Rathour & Narayanan, 2014; Anirudhan & Narayanan, 2015). Under such a postulate, further investigation should be directed towards answering the question regarding what factors regulate the maintenance *vs.* cessation of homeostasis of location-dependent STA spectral selectivity and CDW under physiological and pathological conditions.

Together, our results reveal that changes exclusive to VGIC expression and properties are capable of steering neuronal compartments to span the I–CD continuum and endow these compartments with the potential to perform gamma-frequency coincidence detection. These results imply location-, activity- and behavioural state-dependent dynamic reconfiguration of neuronal kernels and associated CDWs, and our study provides quantitative tools for the systematic assessment of the roles of VGICs and their interactions in effectuating such reconfiguration. Such dynamically reconfigurable feature selectivity and coincidence detection in neurons have important ramifications for state-dependent information processing in neurons, and call for the incorporation of distribution profiles, interactions, neuromodulation and plasticity of different VGICs into the discourse on neural coding and homeostasis (Narayanan & Johnston, 2012).

References

Agmon-Snir H, Carr CE & Rinzel J (1998). The role of dendrites in auditory coincidence detection. *Nature* **393**, 268–272.

Agüera y Arcas B & Fairhall AL (2003). What causes a neuron to spike? *Neural Comput* **15**, 1789–1807.

Agüera y Arcas B, Fairhall AL & Bialek W (2003). Computation in a single neuron: Hodgkin and Huxley revisited. *Neural Comput* **15**, 1715–1749.

Andreasen M & Lambert JD (1999). Somatic amplification of distally generated subthreshold EPSPs in rat hippocampal pyramidal neurones. *J Physiol* **519**, 85–100.

Anirudhan A & Narayanan R (2015). Analogous synaptic plasticity profiles emerge from disparate channel combinations. *J Neurosci* **35**, 4691–4705.

Ascoli GA, Donohue DE & Halavi M (2007). NeuroMorpho.Org: a central resource for neuronal morphologies. *J Neurosci* **27**, 9247–9251.

Astman N, Gutnick MJ & Fleidervish IA (2006). Persistent sodium current in layer 5 neocortical neurons is primarily generated in the proximal axon. *J Neurosci* **26**, 3465–3473.

Bieri KW, Bobbitt KN & Colgin LL (2014). Slow and fast gamma rhythms coordinate different spatial coding modes in hippocampal place cells. *Neuron* **82**, 670–681.

Boehlen A, Henneberger C, Heinemann U & Erchova I (2013). Contribution of near-threshold currents to intrinsic oscillatory activity in rat medial entorhinal cortex layer II stellate cells. *J Neurophysiol* **109**, 445–463.

Buzsaki G (2006). *Rhythms of the Brain*. Oxford University Press, New York.

Buzsaki G (2010). Neural syntax: cell assemblies, synapsembles, and readers. *Neuron* **68**, 362–385.

Buzsaki G & Wang XJ (2012). Mechanisms of gamma oscillations. *Annu Rev Neurosci* **35**, 203–225.

Cantrell AR & Catterall WA (2001). Neuromodulation of Na$^+$ channels: an unexpected form of cellular plasticity. *Nat Rev Neurosci* **2**, 397–407.

Cerda O & Trimmer JS (2010). Analysis and functional implications of phosphorylation of neuronal voltage-gated potassium channels. *Neurosci Lett* **486**, 60–67.

Colbert CM, Magee JC, Hoffman DA & Johnston D (1997). Slow recovery from inactivation of Na$^+$ channels underlies the activity-dependent attenuation of dendritic action potentials in hippocampal CA1 pyramidal neurons. *J Neurosci* **17**, 6512–6521.

Cole KS (1968). *Membranes, Ions and Impulses: A Chapter of Classical Biophysics*. University of California, Berkeley Press, Berkeley.

Cole KS & Baker RF (1941). Longitudinal impedance of the squid giant axon. *J Gen Physiol* **24**, 771–788.

Colgin LL, Denninger T, Fyhn M, Hafting T, Bonnevie T, Jensen O, Moser MB & Moser EI (2009). Frequency of gamma oscillations routes flow of information in the hippocampus. *Nature* **462**, 353–357.

Colgin LL & Moser EI (2010). Gamma oscillations in the hippocampus. *Physiology (Bethesda)* **25**, 319–329.

Crill WE (1996). Persistent sodium current in mammalian central neurons. *Annu Rev Physiol* **58**, 349–362.

Das A & Narayanan R (2014). Active dendrites regulate spectral selectivity in location-dependent spike initiation dynamics of hippocampal model neurons. *J Neurosci* **34**, 1195–1211.

Destexhe A (2010). Inhibitory 'noise'. *Front Cell Neurosci* **4**, 9.

Destexhe A, Rudolph M & Pare D (2003). The high-conductance state of neocortical neurons *in vivo*. *Nat Rev Neurosci* **4**, 739–751.

Dhupia N, Rathour RK & Narayanan R (2015). Dendritic atrophy constricts functional maps in resonance and impedance properties of hippocampal model neurons. *Front Cell Neurosci* **8**, 456.

Dingledine R, Borges K, Bowie D & Traynelis SF (1999). The glutamate receptor ion channels. *Pharmacol Rev* **51**, 7–61.

Engel AK & Singer W (2001). Temporal binding and the neural correlates of sensory awareness. *Trends Cogn Sci* **5**, 16–25.

Enroth-Cugell C & Shapley RM (1973). Adaptation and dynamics of cat retinal ganglion cells. *J Physiol* **233**, 271–309.

Famulare M & Fairhall A (2010). Feature selection in simple neurons: how coding depends on spiking dynamics. *Neural Comput* **22**, 581–598.

Fleidervish IA, Lasser-Ross N, Gutnick MJ & Ross WN (2010). Na^+ imaging reveals little difference in action potential-evoked Na^+ influx between axon and soma. *Nat Neurosci* **13**, 852–860.

Fontaine B, MacLeod KM, Lubejko ST, Steinberg LJ, Koppl C & Pena JL (2014). Emergence of band-pass filtering through adaptive spiking in the owl's cochlear nucleus. *J Neurophysiol* **112**, 430–445.

Freeman WJ (2007). Definitions of state variables and state space for brain–computer interface. Part 1. Multiple hierarchical levels of brain function. *Cogn Neurodyn* **1**, 3–14.

French CR, Sah P, Buckett KJ & Gage PW (1990). A voltage-dependent persistent sodium current in mammalian hippocampal neurons. *J Gen Physiol* **95**, 1139–1157.

Fries P, Nikolic D & Singer W (2007). The gamma cycle. *Trends Neurosci* **30**, 309–316.

Gabor D (1946). Theory of communication. *J Inst Electr Eng* **93**, 429–457.

Gasparini S & Magee JC (2006). State-dependent dendritic computation in hippocampal CA1 pyramidal neurons. *J Neurosci* **26**, 2088–2100.

Gasparini S, Migliore M & Magee JC (2004). On the initiation and propagation of dendritic spikes in CA1 pyramidal neurons. *J Neurosci* **24**, 11046–11056.

Golding NL, Mickus TJ, Katz Y, Kath WL & Spruston N (2005). Factors mediating powerful voltage attenuation along CA1 pyramidal neuron dendrites. *J Physiol* **568**, 69–82.

Golding NL & Oertel D (2012). Synaptic integration in dendrites: exceptional need for speed. *J Physiol* **590**, 5563–5569.

Grossman A & Morlet J (1984). Decomposition of Hardy functions into square integrable wavelet of constant shape. *SIAM J Math Anal* **15**, 723–736.

Hanus C & Schuman EM (2013). Proteostasis in complex dendrites. *Nat Rev Neurosci* **14**, 638–648.

He C, Chen F, Li B & Hu Z (2014). Neurophysiology of HCN channels: from cellular functions to multiple regulations. *Prog Neurobiol* **112**, 1–23.

Higgs MH & Spain WJ (2009). Conditional bursting enhances resonant firing in neocortical layer 2–3 pyramidal neurons. *J Neurosci* **29**, 1285–1299.

Hodgkin AL (1948). The local electric changes associated with repetitive action in a non-medullated axon. *J Physiol* **107**, 165–181.

Hodgkin AL & Huxley AF (1952). A quantitative description of membrane current and its application to conduction and excitation in nerve. *J Physiol* **117**, 500–544.

Hoffman DA & Johnston D (1999). Neuromodulation of dendritic action potentials. *J Neurophysiol* **81**, 408–411.

Hoffman DA, Magee JC, Colbert CM & Johnston D (1997). K^+ channel regulation of signal propagation in dendrites of hippocampal pyramidal neurons. *Nature* **387**, 869–875.

Hong S, Agüera y Arcas B & Fairhall AL (2007). Single neuron computation: from dynamical system to feature detector. *Neural Comput* **19**, 3133–3172.

Hong S, Ratté S, Prescott SA & DeSchutter E (2012). Single neuron firing properties impact correlation-based population coding. *J Neurosci* **32**, 1413–1428.

Hu H, Vervaeke K, Graham LJ & Storm JF (2009). Complementary theta resonance filtering by two spatially segregated mechanisms in CA1 hippocampal pyramidal neurons. *J Neurosci* **29**, 14472–14483.

Hu H, Vervaeke K & Storm JF (2002). Two forms of electrical resonance at theta frequencies, generated by M-current, h-current and persistent Na^+ current in rat hippocampal pyramidal cells. *J Physiol* **545**, 783–805.

Hutcheon B, Miura RM & Puil E (1996). Models of subthreshold membrane resonance in neocortical neurons. *J Neurophysiol* **76**, 698–714.

Hutcheon B, Miura RM, Yarom Y & Puil E (1994). Low-threshold calcium current and resonance in thalamic neurons: a model of frequency preference. *J Neurophysiol* **71**, 583–594.

Hutcheon B & Yarom Y (2000). Resonance, oscillation and the intrinsic frequency preferences of neurons. *Trends Neurosci* **23**, 216–222.

Johnston D & Narayanan R (2008). Active dendrites: colorful wings of the mysterious butterflies. *Trends Neurosci* **31**, 309–316.

Joris PX, Smith PH & Yin TC (1998). Coincidence detection in the auditory system: 50 years after Jeffress. *Neuron* **21**, 1235–1238.

Kalmbach BE, Chitwood RA, Dembrow NC & Johnston D (2013). Dendritic generation of mGluR-mediated slow afterdepolarization in layer 5 neurons of prefrontal cortex. *J Neurosci* **33**, 13518–13532.

Kerti K, Lorincz A & Nusser Z (2012). Unique somato-dendritic distribution pattern of Kv4.2 channels on hippocampal CA1 pyramidal cells. *Eur J Neurosci* **35**, 66–75.

Kim J, Wei DS & Hoffman DA (2005). Kv4 potassium channel subunits control action potential repolarization and frequency-dependent broadening in rat hippocampal CA1 pyramidal neurones. *J Physiol* **569**, 41–57.

Kispersky TJ, Fernandez FR, Economo MN & White JA (2012). Spike resonance properties in hippocampal O-LM cells are dependent on refractory dynamics. *J Neurosci* **32**, 3637–3651.

Kole MH, Hallermann S & Stuart GJ (2006). Single I_h channels in pyramidal neuron dendrites: properties, distribution, and impact on action potential output. *J Neurosci* **26**, 1677–1687.

Lai HC & Jan LY (2006). The distribution and targeting of neuronal voltage-gated ion channels. *Nat Rev Neurosci* **7**, 548–562.

Larkum ME, Nevian T, Sandler M, Polsky A & Schiller J (2009). Synaptic integration in tuft dendrites of layer 5 pyramidal neurons: a new unifying principle. *Science* **325**, 756–760.

Laudanski J, Torben-Nielsen B, Segev I & Shamma S (2014). Spatially distributed dendritic resonance selectively filters synaptic input. *PLoS Comput Biol* **10**, e1003775.

Lisman JE & Jensen O (2013). The theta-gamma neural code. *Neuron* **77**, 1002–1016.

Llinás R, Ribary U, Contreras D & Pedroarena C (1998). The neuronal basis for consciousness. *Philos Trans R Soc Lond B Biol Sci* **353**, 1841–1849.

Llinás RR, Leznik E & Urbano FJ (2002). Temporal binding via cortical coincidence detection of specific and nonspecific thalamocortical inputs: a voltage-dependent dye-imaging study in mouse brain slices. *Proc Natl Acad Sci USA* **99**, 449–454.

Lorincz A, Notomi T, Tamás G, Shigemoto R & Nusser Z (2002). Polarized and compartment-dependent distribution of HCN1 in pyramidal cell dendrites. *Nat Neurosci* **5**, 1185–1193.

Lorincz A & Nusser Z (2010). Molecular identity of dendritic voltage-gated sodium channels. *Science* **328**, 906–909.

Magee JC (1998). Dendritic hyperpolarization-activated currents modify the integrative properties of hippocampal CA1 pyramidal neurons. *J Neurosci* **18**, 7613–7624.

Magee JC (1999). Dendritic I_h normalizes temporal summation in hippocampal CA1 neurons. *Nat Neurosci* **2**, 848.

Magee JC & Johnston D (1995). Characterization of single voltage-gated Na^+ and Ca^{2+} channels in apical dendrites of rat CA1 pyramidal neurons. *J Physiol* **487**, 67–90.

Magee JC & Johnston D (1997). A synaptically controlled, associative signal for Hebbian plasticity in hippocampal neurons. *Science* **275**, 209–213.

Marcelin B, Chauvière L, Becker A, Migliore M, Esclapez M & Bernard C (2009). h channel-dependent deficit of theta oscillation resonance and phase shift in temporal lobe epilepsy. *Neurobiol Dis* **33**, 436–447.

Marder E & Goaillard JM (2006). Variability, compensation and homeostasis in neuron and network function. *Nat Rev Neurosci* **7**, 563–574.

Mato G & Samengo I (2008). Type I and type II neuron models are selectively driven by differential stimulus features. *Neural Comput* **20**, 2418–2440.

Mease RA, Famulare M, Gjorgjieva J, Moody WJ & Fairhall AL (2013). Emergence of adaptive computation by single neurons in the developing cortex. *J Neurosci* **33**, 12154–12170.

Meng X, Huguet G & Rinzel J (2012). Type III excitability, slope sensitivity and coincidence detection. *Discrete Contin Dyn Syst Ser A* **32**, 2729–2757.

Migliore M, Hoffman DA, Magee JC & Johnston D (1999). Role of an A-type K^+ conductance in the back-propagation of action potentials in the dendrites of hippocampal pyramidal neurons. *J Comput Neurosci* **7**, 5–15.

Mishra P & Narayanan R (2015). High-conductance states and A-type K^+ channels are potential regulators of the conductance-current balance triggered by HCN channels. *J Neurophysiol* **113**, 23–43.

Nagel KI & Doupe AJ (2006). Temporal processing and adaptation in the songbird auditory forebrain. *Neuron* **51**, 845–859.

Narayanan R & Johnston D (2007). Long-term potentiation in rat hippocampal neurons is accompanied by spatially widespread changes in intrinsic oscillatory dynamics and excitability. *Neuron* **56**, 1061–1075.

Narayanan R & Johnston D (2008*a*). The ascent of channels with memory. *Neuron* **60**, 735–738.

Narayanan R & Johnston D (2008*b*). The h channel mediates location dependence and plasticity of intrinsic phase response in rat hippocampal neurons. *J Neurosci* **28**, 5846–5860.

Narayanan R & Johnston D (2010). The h current is a candidate mechanism for regulating the sliding modification threshold in a BCM-like synaptic learning rule. *J Neurophysiol* **104**, 1020–1033.

Narayanan R & Johnston D (2012). Functional maps within a single neuron. *J Neurophysiol* **108**, 2343–2351.

Nusser Z (2009). Variability in the subcellular distribution of ion channels increases neuronal diversity. *Trends Neurosci* **32**, 267–274.

O'Leary T, Williams AH, Franci A & Marder E (2014). Cell types, network homeostasis, and pathological compensation from a biologically plausible ion channel expression model. *Neuron* **82**, 809–821.

Pape HC (1996). Queer current and pacemaker: the hyperpolarization-activated cation current in neurons. *Annu Rev Physiol* **58**, 299–327.

Perez-Reyes E (2003). Molecular physiology of low-voltage-activated T-type calcium channels. *Physiol Rev* **83**, 117–161.

Pike FG, Goddard RS, Suckling JM, Ganter P, Kasthuri N & Paulsen O (2000). Distinct frequency preferences of different types of rat hippocampal neurones in response to oscillatory input currents. *J Physiol* **529**, 205–213.

Polsky A, Mel BW & Schiller J (2004). Computational subunits in thin dendrites of pyramidal cells. *Nat Neurosci* **7**, 621–627.

Poolos NP, Migliore M & Johnston D (2002). Pharmacological upregulation of h-channels reduces the excitability of pyramidal neuron dendrites. *Nat Neurosci* **5**, 767–774.

Prescott SA, DeKoninck Y & Sejnowski TJ (2008*a*). Biophysical basis for three distinct dynamical mechanisms of action potential initiation. *PLoS Comput Biol* **4**, e1000198.

Prescott SA, Ratté S, DeKoninck Y & Sejnowski TJ (2006). Nonlinear interaction between shunting and adaptation controls a switch between integration and coincidence detection in pyramidal neurons. *J Neurosci* **26**, 9084–9097.

Prescott SA, Ratté S, DeKoninck Y & Sejnowski TJ (2008*b*). Pyramidal neurons switch from integrators in vitro to resonators under in vivo-like conditions. *J Neurophysiol* **100**, 3030–3042.

Prescott SA & Sejnowski TJ (2008). Spike-rate coding and spike-time coding are affected oppositely by different adaptation mechanisms. *J Neurosci* **28**, 13649–13661.

Pyapali GK, Sik A, Penttonen M, Buzsaki G & Turner DA (1998). Dendritic properties of hippocampal CA1 pyramidal neurons in the rat: intracellular staining in vivo and in vitro. *J Comp Neurol* **391**, 335–352.

Rathour RK & Narayanan R (2012*a*). Inactivating ion channels augment robustness of subthreshold intrinsic response dynamics to parametric variability in hippocampal model neurons. *J Physiol* **590**, 5629–5652.

Rathour RK & Narayanan R (2012*b*). Influence fields: a quantitative framework for representation and analysis of active dendrites. *J Neurophysiol* **107**, 2313–2334.

Rathour RK & Narayanan R (2014). Homeostasis of functional maps in active dendrites emerges in the absence of individual channelostasis. *Proc Natl Acad Sci USA* **111**, E1787–E1796.

Ratté S, Hong S, DeSchutter E & Prescott SA (2013). Impact of neuronal properties on network coding: roles of spike initiation dynamics and robust synchrony transfer. *Neuron* **78**, 758–772.

Remme MW & Rinzel J (2011). Role of active dendritic conductances in subthreshold input integration. *J Comput Neurosci* **31**, 13–30.

Royeck M, Horstmann MT, Remy S, Reitze M, Yaari Y & Beck H (2008). Role of axonal Na$_V$1.6 sodium channels in action potential initiation of CA1 pyramidal neurons. *J Neurophysiol* **100**, 2361–2380.

Rudolph M, Pospischil M, Timofeev I & Destexhe A (2007). Inhibition determines membrane potential dynamics and controls action potential generation in awake and sleeping cat cortex. *J Neurosci* **27**, 5280–5290.

Schiller J, Major G, Koester HJ & Schiller Y (2000). NMDA spikes in basal dendrites of cortical pyramidal neurons. *Nature* **404**, 285–289.

Schiller J, Schiller Y, Stuart G & Sakmann B (1997). Calcium action potentials restricted to distal apical dendrites of rat neocortical pyramidal neurons. *J Physiol* **505**, 605–616.

Senior TJ, Huxter JR, Allen K, O'Neill J & Csicsvari J (2008). Gamma oscillatory firing reveals distinct populations of pyramidal cells in the CA1 region of the hippocampus. *J Neurosci* **28**, 2274–2286.

Shah MM (2014). Cortical HCN channels: function, trafficking and plasticity. *J Physiol* **592**, 2711–2719.

Shah MM, Hammond RS & Hoffman DA (2010). Dendritic ion channel trafficking and plasticity. *Trends Neurosci* **33**, 307–316.

Shah MM, Migliore M, Valencia I, Cooper EC & Brown DA (2008). Functional significance of axonal Kv7 channels in hippocampal pyramidal neurons. *Proc Natl Acad Sci USA* **105**, 7869–7874.

Singer W, Engel AK, Kreiter AK, Munk MH, Neuenschwander S & Roelfsema PR (1997). Neuronal assemblies: necessity, signature and detectability. *Trends Cogn Sci* **1**, 252–261.

Softky W (1994). Sub-millisecond coincidence detection in active dendritic trees. *Neuroscience* **58**, 13–41.

Stuart G, Schiller J & Sakmann B (1997). Action potential initiation and propagation in rat neocortical pyramidal neurons. *J Physiol* **505**, 617–632.

Stuart GJ & Häusser M (2001). Dendritic coincidence detection of EPSPs and action potentials. *Nat Neurosci* **4**, 63–71.

Tallon-Baudry C & Bertrand O (1999). Oscillatory gamma activity in humans and its role in object representation. *Trends Cogn Sci* **3**, 151–162.

Tigerholm J, Migliore M & Fransen E (2013). Integration of synchronous synaptic input in CA1 pyramidal neuron depends on spatial and temporal distributions of the input. *Hippocampus* **23**, 87–99.

Uebachs M, Opitz T, Royeck M, Dickhof G, Horstmann MT, Isom LL & Beck H (2010). Efficacy loss of the anticonvulsant carbamazepine in mice lacking sodium channel β subunits via paradoxical effects on persistent sodium currents. *J Neurosci* **30**, 8489–8501.

Ulrich D (2002). Dendritic resonance in rat neocortical pyramidal cells. *J Neurophysiol* **87**, 2753–2759.

Urdapilleta E & Samengo I (2015). Effects of spike-triggered negative feedback on receptive-field properties. *J Comput Neurosci* **38**, 405–425.

Vacher H, Mohapatra DP & Trimmer JS (2008). Localization and targeting of voltage-dependent ion channels in mammalian central neurons. *Physiol Rev* **88**, 1407–1447.

Vaidya S & Johnston D (2012). HCN channels contribute to the spatial synchrony of theta frequency synaptic inputs in CA1 pyramidal neurons. Program No. 435.15/C58. 2012 Neuroscience Meeting Planner. Society for Neuroscience, New Orleans, LA, USA. Online.

Vaidya SP & Johnston D (2013). Temporal synchrony and gamma-to-theta power conversion in the dendrites of CA1 pyramidal neurons. *Nat Neurosci* **16**, 1812–1820.

Vervaeke K, Hu H, Graham LJ & Storm JF (2006). Contrasting effects of the persistent Na$^+$ current on neuronal excitability and spike timing. *Neuron* **49**, 257–270.

Wang XJ (2010). Neurophysiological and computational principles of cortical rhythms in cognition. *Physiol Rev* **90**, 1195–1268.

Williams SR & Stuart GJ (2000). Site independence of EPSP time course is mediated by dendritic I_h in neocortical pyramidal neurons. *J Neurophysiol* **83**, 3177–3182.

Yu Y & Lee TS (2003). Dynamical mechanisms underlying contrast gain control in single neurons. *Phys Rev E Stat Nonlin Soft Matter Phys* **68**, 011901.

Zemankovics R, Kali S, Paulsen O, Freund TF & Hajos N (2010). Differences in subthreshold resonance of hippocampal pyramidal cells and interneurons: the role of h-current and passive membrane characteristics. *J Physiol* **588**, 2109–2132.

Zhuchkova E, Remme MW & Schreiber S (2013). Somatic versus dendritic resonance: differential filtering of inputs through non-uniform distributions of active conductances. *PLoS One* **8**, e78908.

Additional information

Competing interests

The authors declare that there are no competing interests.

Author contributions

A.D. and R.N. conceived and designed the experiments; A.D. performed the experiments; A.D. and R.N. analysed data. A.D. drafted the article; A.D. and R.N. revised the article critically for important intellectual content; both authors approved the final version.